Measurable fields to spikes causality and its dependence on cortical layer and area.

Shailaja Akella[1], André M. Bastos[2], Earl K. Miller[3], and Jose C. Principe[4]

[1]Allen Institute, Seattle, WA, United States
[2]Department of Psychology and Vanderbilt Brain Institute, Vanderbilt University, Nashville, TN, United States
[3]The Picower Institute for Learning and Memory and Department of Brain and Cognitive Sciences, Massachusetts Institute of Technology, Cambridge, MA, United States
[4]Department of Electrical and Computer Engineering, University of Florida, Gainesville, FL, United States

*Correspondence: shailaja.akella@alleninstitute.org

Abstract

Distinct dynamics in different cortical layers are apparent in both neuronal and local field potential (LFP) patterns. Yet, the associations between spiking activity and LFPs in the context of laminar processing within and across cortices have only been sparingly analyzed. While spike-field connectivity analyses can help decipher the link between the multilevel brain dynamics and behavior, they present a challenging computational problem due to disparities in the signal structure and corresponding signal processing methodologies. Here, we study the laminar organization of spike-field causal flow patterns using a novel multiscale framework that quantifies LFPs as a point process of frequency-specific transient bursts. The framework provides a unifying metric space for computations on both signal modalities while expanding the time resolution to the slowest sampled signal. To quantify directional asymmetries between spikes and LFPs in the point process space, we employed directed information, an information-theoretic measure of causal influence, using techniques from kernel spike-train representations. We analyzed spike-field causal flow within and across individual columns of visual-area 4 (V4) and prefrontal cortex (PFC) in monkeys performing a visual task with modified sample predictability. Our results revealed area and frequency specificity in the laminar organization of spike-field causal connectivities. During stimulus processing, gamma bursts ($40-80$ Hz) in the superficial layers of V4 largely drove intralaminar spiking. These gamma influences also fed forward up the cortical hierarchy, where they modulated laminar spiking in PFC. Connections originating in V4 were generally more pronounced during randomized stimulus presentations than during repeated presentations. In the same interval, we observed a reverse phenomenon in the PFC where the direction of intralaminar information flow was from spikes→fields. Here, superficial-layer neurons were the primary drivers of gamma activity in the same layers, while deep layers neurons modulated beta ($8-30$ Hz) activity in the column. Moreover, these influences dually controlled top-down and bottom-up processing, with neuronal influences being higher to gamma during randomized stimuli and to beta during repeated stimulus presentations. Prestimulus spiking activity in V4 and PFC was primarily driven by deep-layer beta in PFC, and the feedback pathway showed enhanced information transfer during repetitive blocks. Our results not just corroborate existing theories on the functional roles assumed by individual cortical layers but also emphasize the complexities of causal interactions between the two signal modalities. Lastly, the automated nature of the methodologies simplify their application to multiple brain areas and behavior.

1 Introduction

Whereas correlation models describe the dependence structure between observed variables, causal models go one step further: they predict whether a variable directly affects a change in another. Understanding the causal interactions between neural entities is central to studying brain function. In this pursuit, several statistical methods have been developed at each scale of the electrophysiological measures - spiking and local field potentials (LFPs). In LFPs, Granger causality studies have implicated distinct frequency bands in several neurophysiological phenomena, including predictive routing (Pelt

et al. 2016; André M Bastos, Lundqvist, et al. 2020), top-down and bottom-up signal processing (Gregoriou et al. 2009; Andre Moraes Bastos et al. 2015; Richter, Coppola, and Bressler 2018; Ferro et al. 2021), and working memory (Popov, Jensen, and Schoffelen 2018; Dimakopoulos et al. 2022). Pairwise correlations between single neurons have identified network organization consistent with anatomical connectivity (Tanaka 1983; Alonso, Usrey, and Reid 1996; Z. Wang et al. 2013; Siegle et al. 2021; Jia et al. 2022), detected distinct functionally specialized populations (Jia et al. 2022; Semedo et al. 2022), and enabled foundational understanding of behavior encoding processes (Stevenson et al. 2008; Clopath et al. 2010; Cohen and Kohn 2011).

However, studies in individual signal modalities present only a partial explanation of brain function. A single neuron cannot support complex behavior like perception, cognition, action, etc. These capabilities emerge only when networks of neural circuits, as a whole, define specific brain functions. In this view, LFPs that account for the joint activity of neuronal assemblies constitute a critical 'middle ground' between single neuron activity and behavior (Freeman 2000; Buzsaki and Draguhn 2004). To that end, bridging this pathway from brain structure to function requires detailed knowledge of the effective influences across the signal modalities. Yet, the distinct class of spike-field causal analyses is not without challenges. Firstly, spike trains are discrete binary-valued signals modeled as point processes, whereas field potentials are continuous signals preferably analyzed using classical signal processing tools. Secondly, compared with the millisecond dynamics of spiking activity, LFP dynamics vary much too slowly at orders of a few hundred milliseconds. Lastly, it is difficult to completely dissociate spiking-related events from LFPs, eventually contributing to spurious associations between the signals (Ray 2015). These inequalities in the multiscale brain activity call for specialized methodologies that must explicitly incorporate the concepts of neurophysiological signal generation, time resolution in the tens of milliseconds, and a shared metric space between the modalities.

Any construct of an effective cortical network must consider the influence of the anatomical parcellations of its structure. Anatomical tracing studies in the cortex have found that the laminar location of cell bodies and their termination patterns underlies a hierarchical organization of cellular connections (Felleman and Van Essen 1991; Thomson et al. 2002). In other words, its position in the hierarchy affects the diversity of synaptic inputs a neuron receives, correspondingly influencing its functionality. For instance, in many parts of the cortex, areas higher up the hierarchy represent increasingly complex features of the stimuli (visual, Maunsell and Essen 1983; Desimone et al. 1984; Connor, Brincat, and Pasupathy 2007; auditory, Atencio, Sharpee, and Schreiner 2009; Atencio and Schreiner 2010; somatosensory, Iwamura 1998). Even at a global scale, feedforward and feedback connections differentially recruit neuronal populations in a layer-specific manner (Lefort et al. 2009; X.-J. Wang 2010; Markov and Kennedy 2013; André M Bastos, Lundqvist, et al. 2020). Likewise, quantitative modeling efforts of such a hierarchical flow has generated testable predictions. Most noted is the microcircuitry developed by Douglas and Martin (Douglas and Martin 1991) based on their studies in the cat-visual cortex, where their conduction-based connectivity model between the thalamic and cortical neurons formed the basis for canonicity over the cortical sheet. Another prediction borne out of hierarchical quantitative modeling is that the brain may employ empirical Bayesian inference on its sensory inputs (K. Friston 2003, 2008, 2010), providing support for several neural computation theories including predictive coding, hierarchical message passing and mean-field interactions.

Although recent technological advancements in electrode design have enabled simultaneous measurement of neurons and LFPs at multiple, interconnected hierarchical levels, only a few studies have explored their associations while accounting for the hierarchical cortical processes. Noteworthy analyses include those conducted by Buffalo et al. 2011. Here, during a task of directed spatial attention, primate visual areas $1, 2$, and 4 (V1, V2, and V4, respectively) reported significantly different spike-field coherence patterns between the superficial and deep layers. Single neurons coherent with gamma band ($40 - 60$ Hz) frequencies were confined to the superficial layers, while those synchronized with alpha band frequencies ($6 - 16$ Hz) were dominantly found in the deep layers. In areas V2 and V4, spike-field coherence was modulated by attention - decreases in alpha synchrony contrasted with increases in gamma synchrony. While these results set precedence for spike-field association studies in the cortical column, the implemented metrics allowed for correlative but not causal inferences. Further, spectral estimations of LFPs limit access to timing information important to deciphering immediate causal influences between the signals. Lastly, their findings only focused on the visual cortex.

In this work, we address the above challenges by implementing a neurophysiologically relevant interpretation of the LFP traces in terms of their oscillatory burst patterns. Characterized by their timing,

amplitude, and duration, the bursts collectively summarize a marked point process representation of the LFP traces (Akella, Mohebi, Principe, et al. 2021) - therefore, bringing the two modalities into the same algebraic space of point processes while maintaining the fine temporal structure of the oscillations. Next, we introduce an information theoretic metric, directed information, in the point process space enabling causal inferences between the signal modalities. To analyze the specifics of feedforward and feedback spike-field connectivity, we apply our methodologies on layer-resolved, simultaneous recordings of LFPs and spiking activity from the visual and frontal areas of two primates performing a visual task with modulated stimulus predictability. We build on previous analyses conducted on the same dataset(André M Bastos, Lundqvist, et al. 2020) where causal connectivity between LFPs revealed interesting asymmetric networks in the alpha/beta and gamma frequency ranges. Accordingly, we focus our analyses of spike-field causal connectivity with gamma bursts in the $40-80$ Hz frequency range and alpha/beta bursting in a broad frequency range of $8-30$ Hz. These analyses revealed layer and frequency-specific asymmetries in spike-field associations and presented causal evidence for the direction of flow of these signals. The findings suggest a complex dynamic between the two modalities consistent in their asymmetries while revealing a complicated directional influence pattern.

2 Results

2.1 Projection of field potentials onto the point process space

Recognizing the need for simultaneous studies of spiking activity and local field potentials (LFPs), we propose to analyze causal connectivity patterns between the multiscale activity using an event-based quantification of LFPs. Specifically, we summarize each LFP trace as a point process of transient bursts of narrowband oscillations in established frequency ranges (beta, 8 - 30 Hz, and gamma, 40 - 80 Hz). The resulting representation allows for a unified metric space between spiking activity and LFPs while preserving the time resolution across the different recording modalities. To realize such a representation, we developed an unsupervised learning model, called the generative model for oscillatory bursts (Akella, Mohebi, Principe, et al. 2021). Unlike other time-frequency decomposition techniques, the generative model explicitly incorporates the concepts of neurophysiological signal generation and enables a high time resolution representation of transient activity. The model achieves this by isolating oscillatory waveforms from the spontaneous activity of bandpassed LFPs used as training data. Using sparse coding techniques, these waveforms are later optimized to compile a dictionary of representative oscillatory waveforms. The final point process representation of the test signals is then supplied by a convolution between each bandpassed LFP trace and the learned dictionary, followed by an adaptive threshold on burst power for event identification (Figure 1**A**).

To examine the role played by oscillatory dynamics in sensory information processing, we fit the generative model to laminar LFPs recorded from visual area 4 (V4) and prefrontal cortex (PFC) in two monkeys while they were actively engaged in a delayed match to sample (DMS) task (Figure 1**C**, bottom). In each session of the DMS task, the predictability of the stimulus was additionally modified every 50 trials in one of two ways: 1) the same stimulus was cued in consecutive trials during repetitive trial blocks, and 2) a randomly sampled stimulus was cued in consecutive trials during randomized trial blocks (Figure 1**C**, top). Across ten sessions and two monkeys, we analyzed LFPs in the gamma ($40-90$ Hz) and beta ($8-30$ Hz) frequency ranges. Learning on the model was performed specific to the area and in a session-wise manner, culminating in 4 dictionaries per session (2 areas and 2 frequencies). Example waveforms from each dictionary are summarized in Figure S1.

The main advantage of a point process representation of LFPs resides in its interpretability via rasters and rate plots. While the former supplies a platform for identifying precise timing-based modulations, the latter enables inferences based on the general properties of the point process. Figures 1**D,E** present representative rasters and rate functions over the complete trial duration for all signal modalities in area V4 (PFC, Figure S4). For better visualization, we plot rasters of beta and gamma bursts to demarcate each oscillatory peak. These plots succinctly summarize associations observed in previous studies (André M Bastos, Loonis, et al. 2018; André M Bastos, Lundqvist, et al. 2020; Lundqvist, André M Bastos, and Miller 2020) between spiking and gamma activity ($r_{V4} = 0.66$, $r_{PFC} = 0.93$, $p < 0.05$) and their anti-correlation with beta bursting (neuron, $r_{V4} = -0.62$, $r_{PFC} = -0.13$, $p < 0.05$; gamma, $r_{V4} = -0.50$, $r_{PFC} = -0.19$, $p < 0.05$). This anti-correlation between the low and high-frequency signals can be associated with the task. Increased spiking activity and gamma

bursting are observed during bottom-up processing tasks, i.e., during sample and response intervals. Whereas activity in the beta frequency range is higher in the delay period during which top-down processing streams are more active.

To further validate the burst detections made by the generative model, we replicate results from a previous study (André M Bastos, Lundqvist, et al. 2020) on the same dataset. For this, during the fixation and sample intervals, we analyzed the effect of stimulus predictability on gamma and beta power in V4 and PFC (Figure S2). Power fluctuations in each frequency range are determined by weighing the intensity function of the point process by the local power in the oscillatory burst (See methods, 4.2.1). These burst power functions differ from burst rate functions in that they also capture the local power fluctuations in transient LFP activity. The high time resolution of the LFP point process allows for sample-by-sample significance analysis of the power functions enabling additional inference on the timing of the power modulations. Throughout the sample interval, we observed increased gamma activity in V4 to randomized stimuli (Figure S2**A**, right). Moreover, superficial layer gamma power in the early sample period noted more significant increases than the deep layer gamma power ($p < 0.05$, ANOVA). Gamma band power in the PFC was not modulated by sample predictability. Opposite effects were observed in the beta band power, where over the cortical columns of V4 and PFC, beta power increased during repeated stimulus presentations ($p < 0.01$, ANOVA). In this case, beta power modulations to sample predictability was more prominent in the deep layers than in the superficial layers across both cortical areas ($p < 0.05$, ANOVA). Moreover, this layer specialization of beta activity was observed only in the later half of the sample interval. In the fixation interval, the effect of stimulus predictability was most pronounced in the early periods, where beta power modulations in the deep layers of V4 were significantly higher (ANOVA, $p < 0.01$) during repeated presentations of the stimulus.

These results along with the results from (André M Bastos, Lundqvist, et al. 2020) provide strong evidence for the involvement of oscillatory LFP rhythms in bottom-up and top-down information processing, where the separate pathways involving distinct cortical layers, timings, and frequencies point to a hierarchical system that mediates information integration.

2.2 Visual stimulation reorganizes baseline network connectivity

Using directed information (DI) estimates, we identify direct causal influences between neurons in individual cortical columns of V4. DI is an information-theoretic measure that quantifies the magnitude and direction of information flow from one random variable to another. An improvement over mutual information (equation 10), DI identifies causal influences between variables by limiting the support of the causal variable only up to the current timestamp (equation 11). For our formulation of DI, we combine techniques from information theory and kernel-based spike train representations, where we circumvent tedious probability estimations for the entropy measure using a functional interpretation approach (Figure 1**B**, equations 13 - 16). Additionally, the formulation allows for DI estimation in a trial-wise manner.

Across neurons within the same cortical column, direct causal influences were identified in 2 steps (Figure 2**A**). First, we eliminated connections with non-significant DI by testing against the null hypothesis of non-causality ($p < 0.05$, $N = 100$ randomizations). To construct the surrogate data for the null hypothesis, we destroyed the causal structure between neural activity by repeatedly shuffling the spiking activity of the causal neuron. Next, direct influences in the neural network were teased apart from indirect influences by conditioning DI on 'side variables' (equation 12) in identified cascading and proxy topological connections within the network (see Methods). This is an important step for neuroscientific studies, especially in the visual cortex, where neuronal networks are heavily recurrent in their connectivity. It must be noted that although DI does not determine the excitatory or inhibitory nature of the connection, it is able to recognize both types of influences (Methods, Figure S3).

To determine whether the neuronal interaction patterns change over the course of the trial, we separately analyze direct causal influences in the fixation and early sample interval, [0-0.5]s. Figure 2**B** uses directed graphs to summarize the general causal connectivity in the V4 cortical column across subjects for each task interval. Each edge and its direction is identified by aggregating the identified causal connections in individual cortical columns, while the edge weights are constructed to describe the strength of the connection as the averaged DI over all direct connections. Across fixation and sample intervals, we observed a reversal in the within-column causal influence patterns in V4. During fixation, the dominant pathway of causal influence included the deep $\rightarrow$ superficial and the deep $\rightarrow$

deep layer connections. The effect was two-fold where the increased influence of deep layer neurons on the cortical column was evident via increases in DI (ANOVA, $p < 0.001$) and an increased proportion of connections originating from the deep layers (Figure 2**C, B-**inset). By contrast, during sample presentation, driver neurons were largely concentrated in the superficial layers where this reversal was marked by an increased proportion of connections originating from the superficial layer neurons and their strength (ANOVA, $p < 0.001$).

Overall, superficial layer neurons were more specialized in processing information during the sample period, while deep layer neurons directed information processing during fixation. Additionally, in line with anatomical projection patterns, these findings suggest that superficial layers support feedforward pathways channeling information from lower to higher-order cortical areas, while feedback pathways are supported by deep layers.

2.3 Gamma bursts are the earliest visual response in V4

Using the high time resolution of the LFP point process, we compared the temporal latency of stimulus-evoked responses in bursting activity with that of spiking in V4 in a trial-wise manner. For this, we considered bursts during the initial 200 ms of the sample interval. In each trial, we noted the response latency of beta and gamma activity as the start time of the earliest burst that appeared during the 200 ms interval. Start time of each burst considers the burst length, L, (see Methods, 4.2.2) and is selected as $t = L/2 - \tau$s, where τ is the time-point corresponding to the center of the burst. For spiking activity, we estimated trial-wise response latencies as the time of the first spike in a 20 ms window around the neuron's maximum response in the 200 ms interval. Figure 3**A** summarizes the latency quantification for gamma and spiking activity in an example trial. Statistical analysis of the onset times across the signal modalities revealed significantly different latencies (Figure 3**B**, ANOVA, p $< 1e^{-3}$). In the majority of trials, the first gamma bursts appeared 50 ms post-stimulus presentation, while the first spiking responses appeared 98 ms post-stimulus presentation - registering an $\sim$ 50 ms delay between the first gamma event and spiking responses in V4. Lastly, beta bursts were fewer, much delayed, and were most likely to appear after spiking activity at 160 ms post-stimulus presentation. Overall, the succession of responses followed the order of gamma, spiking, and, finally, beta activity.

Next, we tested if stimulus predictability impacted the onset times of oscillatory and spiking activity in V4 (Figure 3**C**). Since beta activity was sparse in the initial 200 ms, we relaxed the constraint on beta burst timings and considered the start times of the first beta burst over the entire sample interval. Additionally, we identified second gamma bursts as those that followed gamma events in the initial 200 ms. To determine the time-dependency of evoked responses on stimulus predictability, we analyzed the onset latencies of spiking activity, first gamma, second gamma, and first beta event, separately in the repetitive and randomized trial blocks. The first spiking and gamma events were strongly locked to the stimulus and were not affected by stimulus predictability (ANOVA, gamma, p = 0.51; spiking, p = 0.3). However, the first beta burst and the second gamma burst showed significant modulations (ANOVA, p< 0.001). During repeated presentations of the stimulus, the first beta burst appeared $\sim$ 15 ms earlier as compared to when the stimuli were randomly presented. The reverse was observed in the timings of the second gamma burst; these events appeared earlier during the randomized trial blocks by $\sim$ 12 ms than in the repetitive blocks.

Given the order of stimulus-evoked responses across bursts and spiking activity, we set up DI to measure the layer-wise causal influence of gamma bursts on spiking activity during the early sample interval of [0 - 0.5s]. We observed a strong influence of gamma bursting on spiking that was largely confined to the superficial layers (ANOVA, p < 0.001, Figure 4**B**). These influences were largest between superficial $\rightarrow$ superficial and superficial $\rightarrow$ deep layers (ANOVA, p < 0.001, Figure S6**A1** middle), similar to the single neuron connectivity patterns in the same interval (Figure 2**C**, right panel). Building upon the response latencies, we next analyzed the layer-wise causal influence of spiking activity on beta bursting. Spiking activity in the deep layers had a larger causal influence on beta activity in the cortical column (ANOVA, p < 0.001, Figure S5), but the influences were weak in general. These results are in line with previous reports on oscillatory responses in the visual cortex where spike to gamma coherence was found to be largest in the superficial layers, and spike to beta coherence in the deep layers (Roopun et al. 2008; Maier et al. 2010; Buffalo et al. 2011; André M Bastos, Lundqvist, et al. 2020). Overall, these findings suggest a systematic causal interplay between spikes and fields that may further aid information integration within and across specialized cortical areas.

2.4 Spike-field interactions display consistent layer and frequency specialization but dynamic directionality across areas

Within individual columns of V4 and PFC, we were interested in quantifying the directional asymmetries between spike-field influences. To analyze their variations over different tasks, we separately analyzed activity in the fixation ([-1 - 0s]), and sample period ([0 - 1s]). We further split the sample interval into early ([0 - 0.5s]) and late ([0.5 - 1s]) sample periods to account for the timing differences noted in the dynamics of gamma and beta power functions (Figure S2). Across DI estimates evaluated in individual cortical columns, the dominant causal influence between spiking activity and LFPs was identified by comparing the DI estimates in the opposite directions. These results are summarized using directed graphs as shown in Figure 4**C, D**, where each edge is weighted by the difference in DI between the counter-influences, ΔDI. The edges are color-coded to represent the dominant causal variable between spikes and fields.

In V4, we found that field potentials largely drove spiking activity ($p < 0.001$, Cohen-d > 0.2, Figure 4**C**), while the frequencies involved correlated with the different tasks. During fixation, both beta and gamma strongly influenced spiking activity, while only gamma bursts drove spiking in the sample intervals (Figure 4**C**, top row). On resolving these connections into the different cortical layers, we found interesting patterns of layer specialization in the beta and gamma causal connectivities. In the fixation interval, beta bursting in both the deep and superficial layers significantly affected spiking activity, where these influences were strongest from the deep layers to the superficial layers (ANOVA, $p < 0.001$, Figures 4**C** column 1). The layer specialization of beta influence on spiking activity approximately mimicked that reported in spike-spike causal connections in the same interval (Figures 2**C** left, S6**A2** left), although superficial beta activity had no significant influence on deep layer spiking. Across all analyzed task intervals, superficial-layer gamma activity maintained a strong influence on spiking in the superficial layers that significantly increased upon sample presentation and remained high through the sample interval (ANOVA, $p < 0.001$). Specifically, a primary difference between spike-field interactions in the early and late sample periods was the activation of deep layer gamma activity that exerted increased influences on deep and superficial layer spiking (ANOVA, $p < 0.001$). Among these, deep gamma activity more strongly modulated superficial spiking in the column. A similar pattern was also observed in gamma $\rightarrow$ spike connectivity during fixation.

While neurons in V4 were primarily driven by field potentials, driver signals in PFC switched roles between LFPs and spiking over different task intervals. Similar to V4, beta bursts induced spiking activity in PFC during fixation, where these causal influences were significantly higher in PFC than in V4 (ANOVA, $p < 0.001$). Also, influences between gamma and spiking were absent in the PFC during fixation. During the late sample period, this directionality of influence reversed such that spiking activity induced beta and gamma bursting in the column (Figure 4**D**, top row). Moreover, in the early sample period, the stimulus did not evoke any spike-field causal interactions in PFC. Analysis of layer-wise causal connectivity patterns in PFC revealed consistent frequency specialization with that of V4. In the fixation interval, deep beta activity strongly influenced spiking in the column (ANOVA, $p < 0.001$, Figure 4**A, D** column 1). Superficial beta activity also exerted significant modulations on laminar spiking activity, however, the influences were weaker (ANOVA, $p < 0.001$). Despite the reversal in directionality in the late sample period, neurons in the column drove gamma activity in the superficial layers, with the strongest influences coming from neurons in the superficial layers. While superficial layer neurons affected both gamma and beta bursting, the impact was significantly lower on beta activity (ANOVA, $p < 0.001$). As expected, spiking $\rightarrow$ beta influences were highest from the deep layers (ANOVA, $p < 0.001$ Figure 4**D** column 3).

To determine whether the between-area laminar organization of spike-field communications adopts a similar specialization, we next analyzed interlaminar connectivity between V4 and PFC over the different task intervals. Similar to the analysis on intralaminar connectivity, we identified causal influences as those connections with a significantly asymmetric DI estimate. For the purpose of representation, we constructed wheel plots to summarize the inter-area spike-field causal influence patterns (Figure 5). Edges between the modalities are weighted by the difference in DI estimates of the opposite directions. Additionally, each edge is color-coded to correspond to the dominant directionality of causal influence between feedforward (i.e., red, V4 $\rightarrow$ PFC) and feedback (blue, PFC $\rightarrow$ V4).

During fixation, overall feedback causal influences were larger than feedforward (ANOVA, $p < 0.001$, S7 left), where beta activity drove all prestimulus influences (Figure 5**B** left, S7 left). In the feedback direction, beta activity in PFC showed causal connectivity with spiking in V4, whereas

feedforward beta in V4 weakly modulated spiking in PFC (ANOVA, $p < 0.001$, Cohen-d > 0.2). Interestingly, both signals primarily originated in the deep layers of the respective areas (ANOVA, $p < 0.001$) and equally affected spiking in the deep and superficial layers (ANOVA; feedback, $p = 0.1$; feedforward, $p = 0.56$). During stimulus processing, inter-laminar connections were predominantly feedforward such that gamma activity in V4 modulated spiking in PFC (Figure 5**A**, columns 2-3, ANOVA, $p < 0.001$, Cohen d > 0.2). A layer-wise comparison of DI estimates of the opposite directions revealed a strong influence of superficial gamma activity on spiking in the superficial layers of PFC (ANOVA, $p < 0.001$, S7 **A** columns 2-3) in both the early (Figure 5**B**, right) and late sample periods. However, the strength of feedforward causal connectivity between the areas reduced over the sample interval such that stronger connections were observed in the early periods of stimulus processing. In the late sample period, feedforward gamma $\rightarrow$ spike connectivity was additionally accompanied by feedback connections between spiking activity in PFC and beta bursting in V4. In accordance with intralaminar connections in PFC, the directionality of feedback influence was from spikes $\rightarrow$ fields such that neurons in PFC maximally modulated deep layer beta bursting in V4 (Figure 5**A**).

2.5 Stimulus predictability modulates spike-field interaction patterns

We next investigated the spike-field asymmetries that manifest in response to variation in sample predictability. We hypothesized that 1) repeated predictable samples would recruit feedback pathways inducing top-down processing, and 2) stimulus-processing of randomized unpredictable samples would evoke signals that are fed forward up the cortical hierarchy, distilling the information in a bottom-up fashion. To test these hypotheses, we compared the DI estimates evaluated in the repetitive and randomized trial blocks across previously identified significant causal connections between spikes and fields. For ease of interpretation, we adapted similar representation styles as in the previous sections (Figure 6). Here, edges are weighted by ΔDI, which corresponds to the difference between the DI estimates in randomized and repetitive trial blocks. While we maintained the directionality of influence from the previous sections, each edge is color-coded to represent the stimulus type of higher DI for that specific connection.

Intralaminar spike-field causal connectivity in V4 was higher during randomized stimulus presentations (Figure 6 **B**, S8**A**). In the early sample interval, these unpredictable stimuli enhanced the intralaminar connectivity between gamma $\rightarrow$ spike in V4, where the most significant increments were in the connectivity between superficial layer gamma to deep layer neurons (ANOVA, $p < 0.001$, 6**A**, 6**B** middle, S8**A** middle). On the contrary, causal influences in the late sample period were most significantly enhanced between deep gamma $\rightarrow$ superficial spiking in the randomized trial blocks (ANOVA, $p < 0.001$, 6**B** right, S8**A** right). During fixation, the effect of deep layer beta activity on spiking was weakly higher to these unpredictable stimuli (6**B** left, S8**A** left). Modulations in PFC connectivity to sample predictability were only observed in the late sample period and only in the connections from spike$\rightarrow$field (6**C** right, S8**B**). Moreover, these influences had a dual response to stimulus predictability, with neuronal connectivity being higher to superficial-layer gamma during randomized stimuli (ANOVA, $p < 0.001$) and to deep layer beta during repeated stimulus presentations (ANOVA, $p < 0.001$).

Analysis of interlaminar connections between V4 and spiking showed a clear separation in connectivity between top-down and bottom-up processing (Figure 6**D**). While feedforward connections reported significantly larger causal influences during processing of unpredictable randomized stimuli, all feedback connectivity was enhanced when the stimulus was predictable. Interestingly, feedforward connections during fixation did not display specific modulation to stimulus predictability. In the early sample period, feedforward connections between gamma in V4 to spiking in PFC were most significantly enhanced over pathways culminating in the superficial layers of PFC that largely originated in the superficial V4 (ANOVA, $p < 0.001$, Figures 6**D** top-middle, S9**A** middle). Whereas in the late sample period, this increase in feedforward connectivity between gamma and spiking was strongest along the pathways originating in the deep layers of V4 and innervating superficial PFC (ANOVA, $p < 0.001$, Figures 6**D** top-right, S9**A** right). Feedback connections were strengthened when the sample was predictable. During fixation, repeated stimulus presentations enhanced connectivity between deep layer beta activity in PFC and spiking in the superficial layers of V4 (ANOVA, $p < 0.05$, Figures 6**D** bottom-left, S9**B** left). While, no feedback connections were registered during the early sample period (Figures 6**D** bottom-middle, S9**B** middle), spiking influence of PFC on beta bursting in V4 increased during the late sample period (Figures 6**D** bottom-right, S9**B** right). Similar to connectivity

modulations during fixation, these connections were most significantly modulated along the deep to superficial pathways (ANOVA, $p < 0.05$).

3 Discussion

In this work, we studied the causal dynamics of spike-field interactions by relating spiking activity with oscillatory bursts in the LFPs. Using a novel unifying point process representation for the multiscale brain activity, we undertook a systematic analysis of spike-field connectivity within and across the visual and prefrontal areas. We independently analyzed the spike-field causal flow as the brain switches between two modes of information processing: 1) the bottom-up mode during which novel sensory inputs had to be processed on every trial, and 2) the top-down mode when the same stimulus was presented on every trial alleviating the need to process it. Throughout, spiking activity and LFPs are analyzed in the same Hilbert space, using the same methodologies, time resolutions, and hyperparameters. We also account for the distinct dynamics of neural activity in different cortical layers, task rules, and stimulus types. We find that spike-field communication is more complex than previously assumed (Mitzdorf 1985; Nunez, Srinivasan, et al. 2006; Gong, Li, and Liang 2019) in that it is a dynamic task-modulated relation where field fluctuations do not always reflect the temporal pattern of spiking activity near the electrodes. Spike-field connectivity also adheres to a consistent laminar-specific structure over the cortex in a manner similar to the anatomical hierarchical connections. Specifically, our results reveal two separate communication pathways during top-down and bottom-up information processing: 1) interactions between gamma and spiking that traverse the pathways originating in superficial layers and travel towards superficial layers during behavior that induces bottom-up processing, 2) interactions between beta and spiking activity that originate in the deep layers and travel towards the deep layers during behavior that induces top-down processing. While our results are consistent with previous findings on frequency-specificity (Buschman and Miller 2007; Buffalo et al. 2011; André M Bastos, Lundqvist, et al. 2020), we also demonstrate the dynamic change in interaction patterns with high time resolution. Below we summarize our observations.

LFPs and spike generation: Rooted in the biophysical explanation of LFPs, it is commonly accepted that the oscillatory structures observed ubiquitously in the signal reflect synchronized inputs to a given area (Elul 1972; Logothetis and Wandell 2004). However, it is unclear if LFPs are a mere reflection of synchronization due to an underlying rate modulation or if these oscillations also provide a framework that allows for precisely coordinated spiking as predicted by an active assembly (Buzsáki 2004; Jensen 2006; Canolty et al. 2010). Our results present support for the latter hypothesis. Firstly, the stimulus-related spiking response of single neurons in V4 occurs about mid-way through the first gamma burst in the same area (Figure 3). This observation is in line with neural synchronization models that suggest that optimal communication between two groups of neurons can be achieved when synchronized activity of presynaptic neurons, arriving as bursts at the post-synaptic cell, allow for maximal input density at the target neuron; thereby, eliciting a response (Salinas and Sejnowski 2001; Fries 2005). In V4, this mechanism appears to be implemented by gamma bursts during the early sample period. We speculate that the registered gamma bursts in V4 are not local to the cortical column but may be outputs from presynaptic pyramidal neurons from an upstream area (like V1) or surrounding columns in the visual cortex (Schmolesky et al. 1998; Rasch et al. 2008; Herreras 2016). This result is also in line with response latencies reported in Schmolesky et al. 1998, where engagement of V1 neurons begins around the same time we observed gamma bursts starting to form in V4. The direct effect of gamma bursting on spiking in V4 is later captured as gamma $\rightarrow$ spike influence in our causality analysis (Figure 4**C**). Secondly, layer organization of spike-spike connectivity in V4 mimicked the organization of field $\rightarrow$ spike interactions in the column corresponding to either one of the frequency ranges. These associations are reflective of active engagement of LFPs in coordinating spiking activity. Lastly, 75% of all the significant spike-field causal connectivities identified in the study was directed from fields $\rightarrow$ spikes, suggesting that oscillatory bursts in the LFPs carry information that significantly influences future spike generation.

Frequency specificity of spike-field interactions: Properties of oscillations in the alpha/beta and gamma frequency ranges have implicated their role in gating and control. While ubiquitously observed over the cortex, they are anti-correlated (Jokisch and Jensen 2007; Lundqvist, Rose, et al. 2016, Figure 1**E**). In the visual cortex, gamma power is high and alpha/beta low during sensory stimulation, while the reverse is true when a stimulus is filtered, ignored, or absent (Fries et al. 2001;

Bauer et al. 2006; Buffalo et al. 2011). In PFC, the same frequencies have been implicated in the encoding, maintenance, and read-out of working memory signals (Lundqvist, Rose, et al. 2016; Miller, Lundqvist, and André M Bastos 2018; Akella, Mohebi, Principe, et al. 2021). These findings have led to the general idea that top-down signals are fed back through alpha/beta, and gamma helps maintain the spiking activity carrying sensory inputs, thereby aiding feedforward communication.

In our studies, these specializations broadly translate to spike-field causal connectivity. Generally, connectivity between spiking and alpha/beta activity was observed during fixation and late sample periods, i.e., during the absence and filtering of sensory information. Contrary to beta, connectivity between gamma and spiking was strongest when the subjects were visually stimulated. Local spike-field interactions complemented global interactions showing a similar task-modulated pattern. However, in the late sample period, we found that both alpha/beta and gamma pathways were active simultaneously over local and long-range connections. During this period, gamma bursting in V4 maintained a feedforward influence on spiking activity in PFC which in turn simultaneously controlled gamma and alpha/beta bursting in the PFC column. In the same interval, feedback influences were noted from spiking in PFC that stretched over alpha/beta bursting in V4. Such dual processing in the alpha/beta and gamma pathways implicate a complex system that enables simultaneous local information integration and feedback pathway preparations between higher- and lower-order areas (Choi, Pasupathy, and Shea-Brown 2018). This dual processing period followed after a period of quiescence in the PFC. Throughout the sample period, although V4 gamma maintained a feedforward influence on spiking in PFC, information processing in PFC was only noted in the latter half. These timing delays are within the previously observed ranges for cortico-cortical interactions (Grent-'t-Jong and Woldorff 2007) and represent an activation sequence of key components of the attentional-control brain network. Overall, our findings are suggestive of a signaling system where distinct high and low-frequency signals mediate feedforward and feedback processing, respectively. Herein the top-down effect of alpha/beta bursting helps regulate the processing of bottom-up inputs served by gamma bursts and spiking activity.

Hierarchical organization of spike-field connectivity: Current dogma holds that the cortex is hierarchically organized, where cortical areas are classified by their laminar origin and termination patterns (Callaway 1998; Andre M Bastos et al. 2012; Harris et al. 2019). In this view, feedforward connections originate mainly from superficial pyramidal cells and target the middle layers, and feedback connections originate primarily from deep pyramidal cells and target layers other than the middle layers. While the current description is a simplified depiction of the complex brain networks, recent studies have revealed physiological distinctions in layer-wise dynamics. For instance, neuronal synchronization is asymmetrically distributed across cortical layers, wherein superficial layers show higher synchronization and spike-field coherence in the gamma frequencies, while the deep layers prefer lower frequencies (Maier et al. 2010; Buffalo et al. 2011; Xing et al. 2012; André M Bastos, Lundqvist, et al. 2020. Granger-causality studies further support this functional asymmetry, discernable even over long-range, inter-areal connections (Gregoriou et al. 2009; Vezoli et al. 2021). Given ample evidence supporting the role of gamma (resp. alpha/beta) in feedforward (resp. feedback) processing, it is likely that superficial and deep layers constitute functionally distinct processing streams.

We noted the first evidence of the functional separation between layers in the direct causal connectivities of single neurons in the V4 cortical column. While during fixation, we observed more recurrent and lateral connections within the deep layers, the network connections completely reorganized on visual stimulation, predominantly recruiting superficial layer neurons for stimulus processing (Figure 2). This result strongly supports that superficial layers are placed hierarchically lower than deep layers and support feedforward processing. A further distinction between layers was revealed in the dynamic interplay between the low and high-frequency spike-field causal influences. These dynamics were complementary not just in their timings but also in their layer-specific influences. While superficial-layer gamma most strongly influenced spiking in the same layers during feedforward processing, deep-layer beta selectively affected spiking in the deep layers while controlling feedback processing. This layer-specificity of neural rhythms was held even when the directionality of influence reversed in the PFC in the late sample period. Alongside asymmetries in the within-column spike-field causalities, the specializations were consistent over long-range connections between V4 and PFC (Figures 4, 5). Lastly, in the context of hierarchy, it is worth noting that the directionality of influence from spikes $\rightarrow$ fields was only observed in the PFC in the late sample period. While further systematic studies on PFC connectivity with other intermediate areas are required to fully comprehend this observation, these results are promising because of the role of PFC as a source for top-down signals that biases selection

in early visual areas in favor of the attended features (Paneri and Gregoriou 2017).

Relation with predictive coding models: Predictive coding models suggest a gating mechanism, wherein experience generates predictions that attenuate the feeding forward of predicted stimuli while only projecting forward the residual errors of prediction. These unpredicted errors act as updations that correct the internal prediction generation model. While theories on model implementation are varied (R. P. Rao and Ballard 1999; Spratling 2008; Andre M Bastos et al. 2012; Brown and K. J. Friston 2013), our results are most consistent with a neurophysiological explanation based on distinct neuronal rhythms (Arnal and Giraud 2012; Andre M Bastos et al. 2012). These models suggest that superficial gamma activity is responsible for the feedforward projection of prediction errors, and predictions are fed back to the deep layers via an alpha/beta channel. In this framework, predictions act by preparing the alpha/beta channels that actively inhibit the input-processing gamma pathways in the sensory cortex, eventually reducing the feedforward outputs. Therefore, prediction errors result from a lack of inhibition of the feedforward pathways by low-frequency top-down signals rather than from specialized circuits finalizing comparisons between the prediction and inputs.

The unique setup of the current task incorporates modulation of the stimulus predictability in alternating blocks. Since all stimuli were presented at full contrast, and both block types required the subjects to attend to all stimuli, prediction errors are less likely to be modulated by variations in sensory evidence or attentional modulation. The general idea is that unpredictable randomized stimulus presentations would lead to increased prediction errors corresponding to more mismatched inputs and internal predictions, whereas repeated stimuli would require a memory recall and induce fewer prediction errors. In such a case, block-wise analyses of spike-field connectivity revealed frequency-specific associations with stimulus predictability and garnered further evidence for the role of neural oscillations in directing the information flow of prediction signals (Figure 6). Generally, randomized stimulus presentations induced stronger feedforward connectivity between spikes and gamma, while repetitive presentations strengthened the feedback associations between alpha/beta and spiking (Markov, Vezoli, et al. 2014). Across-layer influences were the most affected by modulations in stimulus predictability across local and global networks. However, no specific generalization between layers could be drawn.

Deviations from common generalizations: Not all connectivity between LFP frequencies and spiking strictly adhered to all the above generalizations. Although relatively weak, gamma $\rightarrow$ spiking influences were significant in the V4 columns even in the absence of any visual stimulation (during fixation, Figure 4**C**). Interestingly, this influence of gamma on spiking activity was higher from the deep layers. A similar increase in deep gamma $\rightarrow$ superficial spiking was also observed in the late sample period in V4. Second, contrary to our expectation, we observed feedforward beta $\rightarrow$ spiking influences between V4 and PFC during fixation (Figure 5). And correspondingly, these V4 beta bursts also reported increased influence on local spiking activity during the randomized trial blocks (Figure 6). These deviations suggest that LFP frequencies assume roles that are dynamically changing and are involved in network activity that are more complex than the simple generalizations.

Improvements over other causal inference methods: In computational neuroscience, the assessment of multi-scale causality presents a challenging computational problem because of the widely disparate statistics of spiking and field potential activity. Recently, Granger causality measures have been adapted to study spike-field causality (Zhang et al. 2012; Kang et al. 2017; Hsieh et al. 2018; Gong, Li, and Liang 2019; C. Wang, Pesaran, and Shanechi 2022). While these models were some of the first to achieve causal inference on hybrid neural signals, they are constrained by important limitations. Firstly, all the proposed models assume that the true data-generating process and the corresponding causal effects of the variables on each other are linear, whereas neural activity is a non-linear process. In such a case, the interpretation of the connectivity estimates can be misleading. Our Hilbert space approach for DI estimation extends the linear model mathematics to non-linear modeling in the input space, where the reproducing kernel Hilbert space is able to handle different types of nonlinearities. Second, the timescales of changes in single-unit activity and LFPs vary vastly, and naturally, the limits on the diagnostic model should be set by the fastest time scale, i.e., inferences must operate on signals with millisecond resolution. Studies that derive support from Fourier analysis methods inevitably fail to capture such high-resolution representations (Gabor 1946) due to the trade-offs between time and frequency resolutions (Zhang et al. 2012; Kang et al. 2017; Gong, Li, and Liang 2019). Our causal estimation framework operates on a high time-resolution construct of LFPs based on bursting activity in specific frequency bands, thereby maintaining time resolutions across the signal modalities. While we do not miss important causal events, our causal inference is limited in its

time resolution, wherein the entropy estimator requires enough samples (300 - 500, Giraldo, M. Rao, and Principe 2014) to avoid improper estimations. Third, studies that adopt a modeling approach for causal analyses rely on 'plug-in' estimators where the data is first fit to a model distribution and then plugged into the casuality estimation framework (Hsieh et al. 2018; C. Wang, Pesaran, and Shanechi 2022). Although plug-in estimators are intuitive, estimating the distribution is a hard problem, both parametrically and non-parametrically. While parametric estimators struggle to balance tractability and oversimplification, non-parametric techniques are computationally demanding and susceptible to overfitting. In either case, making an i.i.d assumption on the data is inappropriate for studying causal analysis. Our causal estimation framework does not assume prior information on signal distribution or independence in either modality, making it a data-driven approach. Lastly, most studies on spike-field analysis do not address the non-causal effects of spike-related transients in the LFPs (Ray 2015), thereby leading to spurious causal estimations. In our studies, we incorporate a rigorous characterization of bursting activity in terms of burst structure, signal-to-noise ratio, transiency, and frequency specialization, alleviating the impact of spike-related transients in LFPs. Overall, our approach has the potential to identify functional relations between spikes and fields in a neurophysiologically sound and computationally appropriate manner.

Here, we would also like to emphasize that in the context of brain connectivity patterns, it is generally impossible to distinguish absolute direct influences from indirect influences if not all nodes of the functionally connected network are sampled. While the problem is not theoretical, it has important implications for interpreting neuronal interactions (Sherman and Guillery 2011; Saalmann et al. 2012). Under the circumstances, care must be taken when making causal inferences. Nevertheless, we believe that with increased coverage of the brain areas, methods such as ours and those by others will be crucial in inferring the direct and indirect pathways of brain signaling. Lastly, while the current study only focuses on spike-field interactions in the cortex, it is only a partial representation of all connectivities plausible in the neural substrate. The current framework can seamlessly translate causal relations between single neurons, LFPs, and cross-frequency relations in the LFPs. These analyses will be considered in future studies while also incorporating signals from intermediate areas such as frontal eye fields and posterior parietal areas. These examinations will merit insights into the area-specific properties of spike-field relations and the activation sequence of an attention-driven brain network.

4 Methods

4.1 Experimental Setup

The data analyzed in this study comprised of multi-laminar recordings from the visual area 4 (V4) and prefrontal cortex (PFC) of macaque monkeys (*Macaca mulatta*) trained to perform a delayed match to sample (DMS) task (André M Bastos, Lundqvist, et al. 2020). We analyzed ten-session recordings from two monkeys that performed five sessions each. Subjects were implanted with linear array U and V probes (from Plexon) using a custom-machined carbon PEEK chamber system with its recording wells placed over the visual/temporal and frontal cortex. The center of each chamber was overlaid with the primary recording area of interest and optimized for an appropriate angle for perpendicular recordings relative to the cortical folding. For each session and brain area, the number of laminar probes varied between 1 and 3. Each probe comprised 16 electrodes with an intersite spacing of 100 or 200μm, culminating in a total linear sampling of 3.0 to 3.1 mm on each probe. Channels from the top of the cortex to a depth of 1.2 mm were classified as superficial layer channels, and deep layer channels were those below 1.2 mm. All surgical and animal care procedures were approved by the Massachusetts Institute of Technology (MIT)'s Committee on Animal Care and were conducted in accordance with the guidelines of the National Institute of Health and MIT's Department of Comparative Medicine.

The experiments were conducted inside a sound-proof behavioral testing booth comprising a primate chair placed 50cm away from an LCD monitor (ASUS, Taiwan). Subjects remained seated throughout the session and were trained to perform the DMS task using positive reinforcement. Monkeys that fixated on a point in the center of the LCD screen for a complete duration of 1s were presented with one of three cue objects. The object remained on the screen for 1s and disappeared during the following delay period. In experiments with monkey-2, the delay period lasted for a uniformly picked time interval between $0.5 - 1.2$s, whereas in experiments with monkey-1, the delay period was a fixed time interval of 1s. At the end of the delay period, a search array consisting of the cued item and one or

two confounding objects appeared on the LCD screen, each occupying a different visual quadrant. The distractor and its position were randomly chosen. A successful trial entailed the subject performing a saccade towards the cued object, for which they received a few drops of diluted juice for positive reinforcement. The trial was terminated if the subject broke fixation at any time. For specific details on behavioral performance, please see (André M Bastos, Lundqvist, et al. 2020)). Additionally, the predictability of the cued object was manipulated either with repetitive or randomized cuing. During randomized cuing, the cue was randomly sampled from a set of 3 objects and presented in each trial. Contrarily, repetitive cuing consisted of the same cue presented in each trial. Each block lasted for 50 trials, where the initial cuing-type was randomly chosen. The trial schematic is presented in Fig.1**C**.

Throughout the session, neural activity was recorded with Blackrock headstages (Blackrock Cereplex). The signals were sampled at 30 kHz, and bandpassed between 0.3 Hz and 7.5 kHz using a first-order Butterworth filter. A low-pass Butterworth filter with a cut-off frequency of 250 Hz and sampled at 1 kHz was used to extract the local field potentials. A Plexon offline sorter was used to manually perform spike sorting. For analyses, both field potentials and spiking activity were downsampled to 500Hz.

4.2 Generative Model for Oscillatory Events

A fascinating phenomenon of neural oscillations is the transient structured patterns that appear sparsely through the signal. These patterns of oscillatory bursts are brought about by external inputs that synchronize neural activity in the 'spontaneous' state of the neural dynamics. While spontaneous state activity is characterized by the 1/f power law and follows an approximate Gaussian distribution (Freeman et al. 1975), oscillatory bursts deviate from this 'Normality' and appear as high-amplitude rhythmic activity that wax and wane. The generative model for oscillatory events builds on this two-state hypothesis and further simplifies modeling by operating in parallel on established cortical rhythms of interest (Niedermeyer and Silva 2005). The model defines single-channel, bandpassed traces of neural recordings, $\tilde{y}(t)$, as a linear combination of spontaneous activity, $n_0(t)$ and oscillatory bursts, $\hat{y}(t)$, as shown in (1). Next, the model employs a shot noise model representation (Davenport, Root, et al. 1958) where each burst is re-constructed as the impulse response of a linear filter defined in a clinically established frequency range as shown in (2). The set of filters defines a dictionary of templates, $D = \{d_\omega\}_{\omega=1}^{K}$, where each filter represents a 'typical' temporal-response of population-level synchronization. Consequently, $\{a_i^\omega,\ \tau_i^\omega\}_{i\ =1}^{n_\omega}$ are the projection coefficients and the timestamps of the oscillatory events as classified by the learnt filter d_ω. Throughout the paper, any marked feature denoted without an explicit mention of ω represents the combined set of all features determined by the K filters.

$$\tilde{y}(t) = n_0(t) + \hat{y}(t), \tag{1}$$

$$\hat{y}(t) = \sum_{\omega=1}^{K} \sum_{i=1}^{n_\omega} a_i^\omega d_\omega(t - \tau_i^\omega). \tag{2}$$

The markers of each burst, namely, its time of occurrence (τ_i), maximum amplitude (α_i), specific clinical band frequency (ω) and duration (δ_i) then constitute a Marked Point Process (MPP); wherein lies the model's advantage to characterize the properties of the oscillatory events in a high – resolution representation of channel activity.

The generative model realizes an MPP representation in two phases: 1) a learning phase for estimating the dictionary, D, from the training data; 2) a testing phase for constructing the MPP from the test signals given the dictionary. Firstly, to improve the accuracy of oscillatory event detection, a preliminary step called 'denoising' involves discriminating between the spontaneous and burst states using a correntropy-based clustering technique (Akella and Principe 2019). The method locally differentiates between the two states using the complete probability density information of the local field components, n_0, and $\hat{y}$. In the final step of denoising, a threshold, κ, is evaluated as the minimum norm among the putative oscillatory events. After denoising, learning is implemented by alternating optimizations between sparse coding and (correntropy-based) dictionary-learning, paralleling a K–means clustering algorithm to learn the oscillatory filters in a data-driven fashion. Model training is terminated as a specific number of iterations is reached or when an upper bound on the Frobenius difference norm between successively determined dictionaries is met.

Lastly, the construction of the MPP from the test signals is implemented in a simple and computationally efficient manner. Each filter in the learnt dictionary is convolved in parallel with each individual channel from the test data. Following this, κ is adapted to the test data and thresholding isolates the oscillatory burst events from spontaneous activity in the test data. In this way, the generative model is able to characterize the properties of each oscillatory burst and enable an easily interpretable MPP representation of multi-channel neural data. (Figure 1**A**). Overall, the model derives support from two user-set hyperparameters: 1) the maximum duration of an oscillatory burst event, M, and 2) the number of filters, K, in the dictionary. For specific details of the model, we direct the reader to (Akella, Mohebi, Principe, et al. 2021), and for easy implementation, we link the MATLAB implementation here: https://github.com/shailajaAkella/MPP-EEG_Ver2.

4.2.1 Burst power

A point process representation enables the construction of a rich feature space via appropriate combinations of the marked features by evoking measures and methods from the well-established field of point process systems (Daley, Vere-Jones, et al. 2003). The burst power function is one such construct (Akella, Mohebi, Riels, et al. 2021). It is an extension of the classical intensity function of point processes, wherein the intensity function is weighted by the transient power of the event at its time of occurrence. Given the timings of each oscillatory event, $\tau_k : k = 1, 2, ...N$, the construction of the burst power function is summarized in equations (3–5). First, transient oscillatory power, $P_{\delta_k}(\tau_k)$, is estimated as the norm-square of the signal amplitude values in the duration of the event (equation 3). Next, the power-weighted event trains are aligned to the onset of the stimuli and superimposed to form the marked event density, $\hat{P}_\delta$ (equation 4). Finally, an estimate of the local burst power is obtained via Gaussian kernel smoothing (equation 5).

$$P_{\delta_k}(\tau_k) = \frac{1}{\delta_k} \sum_{n=\frac{-\delta_k}{2}}^{\frac{\delta_k}{2}-1} \tilde{y}^2(\tau_k + n) \tag{3}$$

$$\hat{P}_\delta(t) = \sum_{k=1}^{N} P_\delta(\tau_k)\boldsymbol{\delta}(n - \tau_k) \tag{4}$$

$$\lambda_\alpha(t) = \sum_{n=-\infty}^{\infty} \hat{P}_\delta(n)\kappa_\sigma(t - n) \tag{5}$$

The construct of burst power, which we call M-spectrum, was specifically designed to address a major shortcoming of the time-frequency (TF) methods - quantification of variation in spectral power simultaneously in both frequency and time. Unlike TF methods, the generative model does not impose any fixed structures on the signal, deliberately avoiding sub-sampling in either dimension. Therefore, the M-spectrum, solely built on the power in the burst events preserves complete time information in the frequency range of interest while consistently limiting leakage from power due to background noise (Akella, Mohebi, Riels, et al. 2021).

4.2.2 Burst length

The duration of each oscillatory burst is determined as follows. First, an envelope of the detected event is estimated using Hilbert Transform. Following this, two points of minima on the smoothed envelope that are separated by atleast $M/2$ samples are identified. Finally, the length of the signal between the two minima determines the duration of each burst. The steps are summarized in (6 - 9):

$$e_k[n] = envelope(\hat{y}_k[n]) \quad n = 1, 2, .., M \tag{6}$$

$$s_k[n] = smooth(e_k[n]) \tag{7}$$

$$\{n_j\}_{j=1}^{2} = peaks(-s_k[n], M/2) \quad s.t \quad n1 < n2 \tag{8}$$

$$\delta_k = length(\hat{y}_k[n_1 : n_2]) \tag{9}$$

4.2.3 Parameter selection

The generative model is applied to learn the burst representations from bandpassed traces of LFP recordings in the broad beta (8 - 30 Hz) and gamma (40 - 80 Hz) frequency ranges. Learning is performed specific to the area and in a session-wise manner, culminating in 4 dictionaries (2 areas and 2 frequencies) per session. Zero-phase FIR filtering is utilized to obtain these signals and model training is performed on a single channel (channel at 200 mm depth) which is then excluded from the testing phase. The designed bandpassed FIR filters have the following properties: 1) for the beta band, the center frequency is set at 20 Hz and the filter order is 25, 2) for the gamma band, the center frequency is chosen to be 60 Hz which culminates in a filter of order 11. The filter orders were deliberately kept at a low value to avoid ringing in the filter response. The maximum duration of each event, M, in the beta and gamma frequency ranges are correspondingly set equal to 500 and 100 ms, while the number of basis vectors (dictionary atoms), K, is upper bound to 30 for both. Silverman's rule of thumb for bandwidth size is used to set all kernel bandwidths for the denoising phase (Silverman 2018).

Next, the M-spectrograms are estimated from a point process representation using Gaussian kernels and it is important that the selection of the bandwidth size be neurophysiologically informed. For this, we chose a bandwidth size that approximately covers the duration of the burst event, translating to 50 and 30 ms for beta and gamma bursts, respectively.

4.3 Directed Information Estimation

In information theory, the mutual information (MI) between two processes, X and Y, communicating over a channel with feedback, can be decomposed into two components: one component captures a causal, feedforward or *directed information* (DI) flow, while the other captures a non-causal or a feedback information flow (equation 10) (Amblard and Michel 2012). Therefore, inferences based on MI can be detrimental in brain networks wherein the neural substrate implements distributed recurrent communications.

$$\underbrace{I(X;Y)}_{\textbf{Mutual Information}} = \underbrace{I(X^n \to Y^n)}_{\textbf{Directed Information}} + I(Y^{n-1} \to X^n) \tag{10}$$

A formal definition of directed information between two stochastic processes, X and Y, is shown in equation (11), where X^n denotes a segment of the successive samples of the process, X i.e., $X^n = [X_1, X_2, ..., X_n]$. Unlike MI, the definition of directed information limits the support of X in the right-side term of equation 11 to the current time i, instead of extending the support over the future time points of X. This term is referred to as the 'causal conditional entropy' in analogy with conditional entropy. Lastly, in the absence of a causal influence of X on Y, the causal conditional entropy reduces to an entropy estimation, and therefore, $I(X^n \to Y^n) = 0$.

$$I(X^n \to Y^n) = \sum_{i=1}^{n} \left[H(Y_i|Y^{i-1}) - H(Y_i|Y^{i-1}X^i) \right] \tag{11}$$

Causal conditioning might involve more than one process. For instance, in networks of neurons, the flow of information between two neurons could be mediated by other neurons in the network. Therefore, the contribution from these other time series is included as 'side information' while deciphering direct causal influences between pairs of neurons. The causal conditional directed information for three processes X, Y and Z is, therefore, defined as in equation (12). Here, the number of 'side variables' can be greater than one, however, for our studies, we incorporate only one other time series.

$$I(X^n \to Y^n || Z^n) = \sum_{i=1}^{n} \left[H(Y_i|Y^{i-1}Z^i) - H(Y_i|Y^{i-1}X^iZ^i) \right] \tag{12}$$

Computation of directed information requires a-priori knowledge about the joint probability distribution function of the random variables. However, such information is unknown in most neuroscience

scenarios of ensemble-recorded electrophysiological signals. For our studies on effective connectivity, we adopt an approach that substitutes any estimation of the probability distribution function from the data with functionals. Here, we exploit the properties of a Hilbert space approach where we implement the matrix-based Renyi's α-order entropy proposed in Giraldo, M. Rao, and Principe 2014. The estimator defines entropy over the eigenspectrum of the normalized Gram matrix, which is a Hermitian matrix of the projected data in a reproducing kernel Hilbert space (RKHS). Specifically, the functional definitions fulfill similar axiomatic properties of Renyi's α-order entropy ($\alpha > 0$), which is a generalization over the well-known Shannon's entropy (Rényi et al. 1961). Given a random variable $X = \{x_1, x_2, ..., x_T\}$ and a normalized Gram matrix A evaluated on X using the real-valued positive definite kernel, $\kappa : \mathcal{X} \times \mathcal{X} \mapsto \mathbb{R}$, the matrix-based estimator of Renyi's α-order entropy is given in equation (13),

$$S_\alpha(A) = \frac{1}{1-\alpha}\log_2\left[\sum_{j=1}^{T}\lambda_j(A)^\alpha\right] \tag{13}$$

where $A_{jk} = \frac{1}{T}\frac{K_{jk}}{\sqrt{K_{jj}K_{kk}}}$ and $\lambda_j(A)$ denotes the jth eigenvalue of A. In essence, the kernel-induced mapping of the sample data into the RKHS provides a means for computing the high-order statistics of the data, wherein the eigenspectrum of the estimated Gram matrix quantifies the variations in these higher-order moments. For evaluations of joint entropy, an extension of the matrix-based entropy measure uses Hadamard products to convey the joint representation of two random variables. In this extension, joint entropy between two random variables, X and Y, is defined as in equation 14, where A_x and A_y are normalized Gram matrices evaluated on X and Y, respectively using positive definite kernels, κ_1 and κ_2.

$$S_\alpha(A_x, A_y) = S_\alpha\left(\frac{A_x \circ A_y}{tr(A_x \circ A_y)}\right) \tag{14}$$

Finally, using the above estimator of entropy, directed information can be rewritten as in equations (15-16), where the latter is obtained by expanding the conditional entropy terms.

$$I_\alpha(X^n \to Y^n) = \sum_{i=1}^{n}\left[S_\alpha(Y_i|Y^{i-1}) - S_\alpha(Y_i|Y^{i-1}X^i)\right] \tag{15}$$

$$= \sum_{i=1}^{n}\left[S_\alpha(Y^i) - S_\alpha(Y^{i-1}) - S_\alpha(Y^iX^i) + S_\alpha(Y^{i-1}X^i)\right] \tag{16}$$

While the above approach provides an elegant yet computationally efficient formulation of directed information, we are still faced with the challenge of defining a positive-definite kernel for point processes. Owing to the popularity of neural spike trains, several methods have been proposed to introduce basic structure to the point process space; we focus on methods that utilize kernel constructs. Here, we briefly summarize the approach. Firstly, each point process is brought into the continuous L_2 space as intensity functions via convolutional operators. Next, using an RKHS inducing kernel, $\kappa : \mathcal{X} \times \mathcal{X} \mapsto \mathbb{R}$ and evoking the kernel trick, the inner product of two intensity functions x_1 and x_2 in the RKHS is computed by a scalar evaluation of the kernel in the input space, i.e., $\langle x_1, x_2\rangle_{\mathcal{H}} = \kappa(x_1, x_2)$. In this way, the required normalized Gram matrix, A, is obtained as a symmetric positive semidefinite matrix representing the pairwise inner product of the intensity functions in the Hilbert space. A complete schematic demonstrating the evaluation of the joint entropy term, $S_\alpha(Y^i, X^i)$, is summarized in Figure1**B**, where the time-shifted matrices, M_x and M_y, capture observations from each intensity function.

In this work, we employ the non-linear Schoenberg kernels (with a rectangular window for intensity function) as the most appropriate choice for projections into the RKHS. Firstly, Schoenberg kernels are positive definite kernels - a necessary property for formulating the matrix-based entropy. Second, derived from radial basis functions, these kernels are universal kernels and can provably approximate arbitrary non-linear functions from the point process to the real space. Third, the locality of a rectangular intensity function limits the causal measure to events only within the window reflective of the

memory of the system under study. Finally, in a rigorous simulation study conducted by us (Akella and Principe 2021), these kernels invariably outperformed other positive definite kernels in identifying the correct causal direction. The complete formulation of the kernel for two intensity functions, x and y, is shown in equations (17 - 18). Here, $\mathbb{I}$ is the indicator function, w is the width of the rectangular window, σ_κ is the kernel size, and $\{t_i\}_{i=1}^N$ are the event timings.

$$\kappa^r_{Sch}(x,y) = \exp\Big\{ \int_T -\frac{1}{\sigma_\kappa}(x_1(t) - x_2(t))^2 dt \Big\} \tag{17}$$

$$x_1(t) = \sum_k \mathbb{I}(t_k - w \leq t \leq t_k + w) \tag{18}$$

Overall, we are able to utilize the Hilbert space as an extended functional representation for point process analysis enabling the estimation of directed information for point process systems. Here, we note an important consequence of the estimation of directed information. Although theoretically, the directed information between independent time series is equal to zero, in practice, empirical values are small and non-negative. We address this issue via appropriate significance testing for the signals under analysis. Finally, the MATLAB implementation of our DI model can be found at https://github.com/shailajaAkella/Directed-Information.

4.3.1 Parameter selection:

Our formulation of directed information depends on four hyperparameters: 1) the kernel size (σ_κ), 2) the width of the rectangular window (w), 3) the order α, and 4) memory of the DI measure (n). The kernel size dictates the geometrical extent of the inner product in the RKHS. In all our analyses, the selection of kernel size follows Scott's rule of thumb for density estimation (Scott and Sain 2005). It is important to note that for projections into the same RKHS, the kernel size must be the same for all entropy evaluations. In our studies, this was chosen to be the kernel size of the input causal variable. Next, for each point process of beta, gamma, and spiking activity, the width of the rectangular intensity operator was fixed as 250 ms, 120 ms, and 120 ms, respectively to approximately cover the duration of the oscillatory burst events. Third, the choice of α is associated with the task under study. For emphasis on rare events (i.e., in the tails of the distribution), α must be chosen close to 1 (Giraldo, M. Rao, and Principe 2014), while higher values of α (> 2) characterize modal behavior. In our analysis of effective connectivity, we are interested in sparse transient synchronizations between multiscale activity. Therefore, we set the order α to 1.01. Lastly, to capture signal transmissions occurring at brief timescales, the memory, n, of the DI measure was chosen to be 20 ms. Since each row in the observation matrix M (Figure 1**B**) maximally depends on time delays captured by the rectangular window used for intensity evaluation and the DI memory, the DI estimations culminate in total time dependency of $w + n$. This evaluates to time dependencies of 270 ms for beta and 140 ms for gamma and spiking activities.

4.4 Constructing Causal Graphs

Connectivity between brain structures or 'nodes' can be best visualized via a graphical representation. In our studies of effective connectivity, a 'node' corresponds to an individual neuron (spikes) or neuronal population (fields), and the edges between the nodes refer to the connectivity patterns formed by causal influences. Finally, we represent the directionality of the causal influence as a directed edge between two nodes.

To this end, we have constructed a causal measure that quantifies directed information flow between the cortical nodes whose properties are characterized via a point process. Since, in practice, all estimated DI measures (between causally and non-causally connected nodes) are greater than zero, we have quantified a fully connected directed graph between all observed nodes. Naturally, the next step is the identification of edges that drive significant causal influences. This is a challenging task as significance testing requires knowledge of the probability density function (pdf) of the DI measure under the null hypothesis (non-causality). However, given the statistical variability of neural activity, the null hypothesis distribution is ever-changing and difficult to pin down. Besides, neuronal circuits in the cortex are primarily involved in recurrent connectivity, making it particularly challenging to determine the direct causal influences between single neurons. On the other hand, spike-field interactions will

assume a unidirectional causal effect at a particular time because of the physics of wave propagation in the brain media. Therefore, we account for these differences between spike-spike and spike-field interaction patterns by implementing separate significance testing pipelines for the interaction types.

4.4.1 Spike-Spike interactions

We test the significance of the DI measures for spike-spike interactions using a random permutation procedure to build a baseline null hypothesis distribution. The calculated DI measure from the actual data is then compared against this baseline distribution to assess the significance levels. Specifically, we create a surrogate system by shuffling the spike times of the causal variable. Therefore, the shuffled point process maintains the spike counts in each realization, but any consistent structure in the joint probability distribution between the two-time series is lost. Performing such random shuffling with many different permutations results in a distribution of DI corresponding to the null hypothesis of non-causality. The null hypothesis is rejected if the DI values estimated on the original time series are greater than the baseline threshold at a significance level of $\alpha_s = 0.05$.

Yet, we have not arrived at a meaningful interpretation of the connectivity patterns as neuronal nodes are recurrently connected, creating copious amounts of indirect influences. Indirect influences can be teased apart from direct influences by conditioning on 'side processes' whose knowledge renders the involved processes statistically independent. Two types of indirect influences considered in this study are the 'proxy' and 'cascading' influences (Figure2**A** right). In a proxy influence pattern, process Y_1 influences process Y_2 which in turn drives the process Y_3 (Figure2**A** top-right). The DI measure, in such a case, is very likely to identify an indirect influence of process Y_1 on Y_3. However, the two processes can be rendered statistically independent given causal knowledge of $Y_2 \rightarrow Y_3$. Similarly, in a cascading topology where two processes Y_1 and Y_3 are commonly driven by a third process, Y_2, the indirect connectivity between the two could be accounted for by their dependence on Y_2 (Figure2**A** bottom-right).

Causal conditioning of DI on 'side processes' is performed as shown in equation (12) such that X directly, causally influences Y, iff $I(X^n \rightarrow Y^n || Z^n) > 0$. Nevertheless, the problem of significance testing is also critical to this analysis as the null hypothesis distribution of the conditional DI measure is also changing, and their estimates between independent processes never typically equate to zero. Therefore, to classify the direct connectivities in the network, we evaluate the decrease in estimated influence between two nodes after the introduction of a side variable. Firstly, potential indirect influence patterns are identified as a set of three nodes that create cascading and proxy-type dependencies in the directed graph. Across all combinations of existing dependencies between the three nodes, we evaluate the percentage change in the DI measure upon conditioning on the third node. Across edges terminating on the same node, any edge that registers a significantly larger change in the DI measure rejects the null hypothesis that all connecting edges to the terminating node directly influence it. The edge with the largest change is classified as indirect and removed from the network. It is important to note that our current implementation of causal graph construction can be easily extended to include verifications on more dependencies - the modification will include expanding the number of conditional (side) processes in the causal conditional DI measure. Such an extension will merit future work and will be explored in the next version of the model implementation.

4.4.2 Spike-field interactions

Unlike spike-spike interactions, we assume unidirectional causal influence between spikes and fields. Under this assumption, it is sufficient to compare the DI estimates of the opposing influences, i.e., between DI(spikes $\rightarrow$ fields) and DI(fields $\rightarrow$ spikes), to identify the dominant connection between the signal modalities. Moreover, we account for the effect of a large sample size on significance testing by using both substantive and statistical significance measures to identify causal influences (Sullivan and Feinn 2012). First, we test the hypothesis that the DI measures from the opposing connections are drawn from populations with different means against the null hypothesis that the population means are the same. If the test rejects the null hypothesis at the 1% significance level, we check for substantive significance by evaluating the effect size (η) between the DI measures of the two connectivity groups. To estimate the effect size, we use the Cohen's - d coefficient (equation 20) where ΔDI is the difference between the group means, and s_1 and s_2 are the group standard deviations. Significant causal influences

are determined as those that register effect sizes greater than 0.2, qualifying those connections that report medium to large differences between the two groups ().

$$\eta = \frac{\Delta DI}{s_p} \tag{19}$$

$$s_p = \sqrt{\frac{s_1^2 + s_2^2}{2}} \tag{20}$$

4.5 Simulations:

We tested the model on a six-neuron network model comprising indirect influences, explicit driver neurons, single input neurons, different synaptic transmissions, and simple excitatory connections. Neuronal activity for all neurons was simulated using the Izhikevich neuron model. The Izhikevich model (Izhikevich 2007) is a mathematical model that is able to reproduce the general behavior of the more biophysically accurate Hodgkin-Huxley-type models using a computationally simpler and efficient formulation. The model is defined by a system of two differential equations and several parameters that dictate the properties of spiking. In general, the Izhikevich neuron model is governed by the following set of equations (equations 8.5 and 8.6 in Izhikevich 2007),

$$C\dot{v} = k(v - v_r)(v - v_t) - u + I \tag{21}$$

$$\dot{u} = a\{b(v - v_r) - u\} \tag{22}$$

$$\text{if } v \geq v_{peak}, \text{ then } v \leftarrow c,\ u \leftarrow u + d \tag{23}$$

Here, v is the neuron's membrane potential, and u is the membrane recovery variable. The latter is associated with activation and inactivation of K^+ and Na^+ ionic currents, respectively, that provide negative feedback to the membrane potential. Description of the hyperparameters and their corresponding values for a regular-spiking neuron are listed in Table S1.

Each neuron, $\{n_i\}_{i=1}^{6}$, could be simulated using three types of input current, I_{in} - 1) constant input, 2) uniform input: a uniformly distributed value between $(0 - 150)$ pA, or 2) bursty input: two 150 ms long pulses of 300 pA, each supplied at a random time, interleaved with a uniformly distributed current between $(0 - 150)$ pA. The latter input was supplied to create a system of bursty neurons where only the presynaptic neuron was stimulated in this manner. The postsynaptic neuron, however, received an input of the former type. Specifically, uniform input current was supplied to neurons n_1, n_2, n_3 and n_6. Whereas n_5 received a constant input current of 150 pA, n_4 was simulated to mimic an interneuron such that it received a bursty input current. The magnitude of excitation current, I_e (or inhibition current I_i) from an excitatory neuron (or inhibitory neuron) in a connection was kept constant throughout each simulation. These values were set at $I_e = 350$ pA and $I_i = 180$ pA. The total current, I, supplied to each neuron comprised of I_{in} and $I_{i/e}$. Membrane noise was generated as Gaussian noise and combined with the neuron's membrane potential, v, at each time point. The synaptic delay between any two connected neurons was maintained at 5 ms, and the memory for all DI evaluations was set at 20 ms. Finally, each simulation was run using time bins of 1 ms, trials lasted for about 1s, and a total of 100 trials were simulated.

Figures S3 summarize the results from the analyses in a step-by-step manner, where **A, B** show example spiking activity and network connections, while **C, D** outline the results. The model identified all direct causal patterns where the adjacency matrix comprising all direct and indirect connections is presented in **C**, and the final connection matrix in **D**. Although the current system includes many potentially indirect influences, the causal model only identified three edges to be significant, demonstrating high robustness to spurious causal influences. However, one indirect influence remained post-significance testing for indirect influences - the edge from n_3 to n_6. Inquiries into the methodology revealed that the connection was never checked for indirect influences. This is because the model's current implementation only checks for indirect causal connections between nodes involved in indirect dependencies of length 3. In the present example, neither $\{n_1, n_3, n_6\}$ nor $\{n_5, n_3, n_6\}$ form an undirected cycle among themselves in the estimated connectivity map (Fig.S3**B**). Therefore, these interactions were not considered indirect by the model. Overall, our model achieved a connectivity detection accuracy of 97.2%.

Acknowledgements

The authors declare that they have no affiliations with or involvement in any organization or entity with any commercial or financial interest that could be construed as a potential conflict of interest. This work was supported by the NSF 1631759 (J.C.P), Office of Naval Research N00014-22-1-2453 (E.K.M), and The JPB Foundation (E.K.M.).

Ethics Statement

All procedures involving animals were reviewed and approved by the Massachusetts Institute of Technology (MIT)'s Committee on Animal Care and were conducted in accordance with the guidelines of the National Institute of Health and MIT's Department of Comparative Medicine.

References

Gabor, Dennis (1946). "Theory of communication. Part 1: The analysis of information". In: *Journal of the Institution of Electrical Engineers-part III: radio and communication engineering* 93.26, pp. 429–441.

Davenport, Wilbur B, William L Root, et al. (1958). *An introduction to the theory of random signals and noise*. Vol. 159. McGraw-Hill New York.

Rényi, Alfréd et al. (1961). "On measures of entropy and information". In: *Proceedings of the fourth Berkeley symposium on mathematical statistics and probability*. Vol. 1. 547-561. Berkeley, California, USA.

Elul, Rafael (1972). "The genesis of the EEG". In: *International review of neurobiology* 15, pp. 227–272.

Freeman, Walter J et al. (1975). *Mass action in the nervous system*. Vol. 2004. Citeseer.

Maunsell, JH and DAVID C van Essen (1983). "The connections of the middle temporal visual area (MT) and their relationship to a cortical hierarchy in the macaque monkey". In: *Journal of Neuroscience* 3.12, pp. 2563–2586.

Tanaka, KEIJI (1983). "Cross-correlation analysis of geniculostriate neuronal relationships in cats". In: *Journal of neurophysiology* 49.6, pp. 1303–1318.

Desimone, Robert et al. (1984). "Stimulus-selective properties of inferior temporal neurons in the macaque". In: *Journal of Neuroscience* 4.8, pp. 2051–2062.

Mitzdorf, Ulla (1985). "Current source-density method and application in cat cerebral cortex: investigation of evoked potentials and EEG phenomena". In: *Physiological reviews* 65.1, pp. 37–100.

Douglas, Rodney J and KA Martin (1991). "A functional microcircuit for cat visual cortex." In: *The Journal of physiology* 440.1, pp. 735–769.

Felleman, Daniel J and David C Van Essen (1991). "Distributed hierarchical processing in the primate cerebral cortex." In: *Cerebral cortex (New York, NY: 1991)* 1.1, pp. 1–47.

Alonso, Jose-Manuel, W Martin Usrey, and R Clay Reid (1996). "Precisely correlated firing in cells of the lateral geniculate nucleus". In: *Nature* 383.6603, pp. 815–819.

Callaway, Edward M (1998). "Local circuits in primary visual cortex of the macaque monkey". In: *Annual review of neuroscience* 21.1, pp. 47–74.

Iwamura, Yoshiaki (1998). "Hierarchical somatosensory processing". In: *Current opinion in neurobiology* 8.4, pp. 522–528.

Schmolesky, Matthew T et al. (1998). "Signal timing across the macaque visual system". In: *Journal of neurophysiology* 79.6, pp. 3272–3278.

Rao, Rajesh PN and Dana H Ballard (1999). "Predictive coding in the visual cortex: a functional interpretation of some extra-classical receptive-field effects". In: *Nature neuroscience* 2.1, pp. 79–87.

Freeman, Walter J (2000). "Mesoscopic neurodynamics: from neuron to brain". In: *Journal of Physiology-Paris* 94.5-6, pp. 303–322.

Fries, Pascal et al. (2001). "Modulation of oscillatory neuronal synchronization by selective visual attention". In: *Science* 291.5508, pp. 1560–1563.

Salinas, Emilio and Terrence J Sejnowski (2001). "Correlated neuronal activity and the flow of neural information". In: *Nature reviews neuroscience* 2.8, pp. 539–550.

Thomson, Alex M et al. (2002). "Synaptic connections and small circuits involving excitatory and inhibitory neurons in layers 2–5 of adult rat and cat neocortex: triple intracellular recordings and biocytin labelling in vitro". In: *Cerebral cortex* 12.9, pp. 936–953.

Daley, Daryl J, David Vere-Jones, et al. (2003). *An introduction to the theory of point processes: volume I: elementary theory and methods*. Springer.

Friston, Karl (2003). "Learning and inference in the brain". In: *Neural Networks* 16.9, pp. 1325–1352.

Buzsaki, Gyorgy and Andreas Draguhn (2004). "Neuronal oscillations in cortical networks". In: *science* 304.5679, pp. 1926–1929.

Buzsáki, György (2004). "Large-scale recording of neuronal ensembles". In: *Nature neuroscience* 7.5, pp. 446–451.

Logothetis, Nikos K and Brian A Wandell (2004). "Interpreting the BOLD signal". In: *Annu. Rev. Physiol.* 66, pp. 735–769.

Fries, Pascal (2005). "A mechanism for cognitive dynamics: neuronal communication through neuronal coherence". In: *Trends in cognitive sciences* 9.10, pp. 474–480.

Niedermeyer, Ernst and FH Lopes da Silva (2005). *Electroencephalography: basic principles, clinical applications, and related fields*. Lippincott Williams & Wilkins.

Scott, David W and Stephan R Sain (2005). "Multidimensional density estimation". In: *Handbook of statistics* 24, pp. 229–261.

Bauer, Markus et al. (2006). "Tactile spatial attention enhances gamma-band activity in somatosensory cortex and reduces low-frequency activity in parieto-occipital areas". In: *Journal of Neuroscience* 26.2, pp. 490–501.

Jensen, Ole (2006). "Maintenance of multiple working memory items by temporal segmentation". In: *Neuroscience* 139.1, pp. 237–249.

Nunez, Paul L, Ramesh Srinivasan, et al. (2006). *Electric fields of the brain: the neurophysics of EEG*. Oxford University Press, USA.

Buschman, Timothy J and Earl K Miller (2007). "Top-down versus bottom-up control of attention in the prefrontal and posterior parietal cortices". In: *science* 315.5820, pp. 1860–1862.

Connor, Charles E, Scott L Brincat, and Anitha Pasupathy (2007). "Transformation of shape information in the ventral pathway". In: *Current opinion in neurobiology* 17.2, pp. 140–147.

Grent-'t-Jong, Tineke and Marty G Woldorff (2007). "Timing and sequence of brain activity in top-down control of visual-spatial attention". In: *PLoS biology* 5.1, e12.

Izhikevich, Eugene M (2007). *Dynamical systems in neuroscience*. MIT press.

Jokisch, Daniel and Ole Jensen (2007). "Modulation of gamma and alpha activity during a working memory task engaging the dorsal or ventral stream". In: *Journal of Neuroscience* 27.12, pp. 3244–3251.

Friston, Karl (2008). "Hierarchical models in the brain". In: *PLoS computational biology* 4.11, e1000211.

Rasch, Malte J et al. (2008). "Inferring spike trains from local field potentials". In: *Journal of neurophysiology* 99.3, pp. 1461–1476.

Roopun, Anita K et al. (2008). "Period concatenation underlies interactions between gamma and beta rhythms in neocortex". In: *Frontiers in cellular neuroscience*, p. 1.

Spratling, Michael W (2008). "Reconciling predictive coding and biased competition models of cortical function". In: *Frontiers in computational neuroscience*, p. 4.

Stevenson, Ian H et al. (2008). "Inferring functional connections between neurons". In: *Current opinion in neurobiology* 18.6, pp. 582–588.

Atencio, Craig A, Tatyana O Sharpee, and Christoph E Schreiner (2009). "Hierarchical computation in the canonical auditory cortical circuit". In: *Proceedings of the National Academy of Sciences* 106.51, pp. 21894–21899.

Gregoriou, Georgia G et al. (2009). "High-frequency, long-range coupling between prefrontal and visual cortex during attention". In: *science* 324.5931, pp. 1207–1210.

Lefort, Sandrine et al. (2009). "The excitatory neuronal network of the C2 barrel column in mouse primary somatosensory cortex". In: *Neuron* 61.2, pp. 301–316.

Atencio, Craig A and Christoph E Schreiner (2010). "Columnar connectivity and laminar processing in cat primary auditory cortex". In: *PLoS One* 5.3, e9521.

Canolty, Ryan T et al. (2010). "Oscillatory phase coupling coordinates anatomically dispersed functional cell assemblies". In: *Proceedings of the National Academy of Sciences* 107.40, pp. 17356–17361.

Clopath, Claudia et al. (2010). "Connectivity reflects coding: a model of voltage-based STDP with homeostasis". In: *Nature neuroscience* 13.3, pp. 344–352.

Friston, Karl (2010). "The free-energy principle: a unified brain theory?" In: *Nature reviews neuroscience* 11.2, pp. 127–138.

Maier, Alexander et al. (2010). "Distinct superficial and deep laminar domains of activity in the visual cortex during rest and stimulation". In: *Frontiers in systems neuroscience* 4, p. 31.

Wang, Xiao-Jing (2010). "Neurophysiological and computational principles of cortical rhythms in cognition". In: *Physiological reviews* 90.3, pp. 1195–1268.

Buffalo, Elizabeth A et al. (2011). "Laminar differences in gamma and alpha coherence in the ventral stream". In: *Proceedings of the National Academy of Sciences* 108.27, pp. 11262–11267.

Cohen, Marlene R and Adam Kohn (2011). "Measuring and interpreting neuronal correlations". In: *Nature neuroscience* 14.7, pp. 811–819.

Sherman, S Murray and RW Guillery (2011). "Distinct functions for direct and transthalamic corticocortical connections". In: *Journal of neurophysiology* 106.3, pp. 1068–1077.

Amblard, Pierre-Olivier and Olivier JJ Michel (2012). "The relation between Granger causality and directed information theory: A review". In: *Entropy* 15.1, pp. 113–143.

Arnal, Luc H and Anne-Lise Giraud (2012). "Cortical oscillations and sensory predictions". In: *Trends in cognitive sciences* 16.7, pp. 390–398.

Bastos, Andre M et al. (2012). "Canonical microcircuits for predictive coding". In: *Neuron* 76.4, pp. 695–711.

Saalmann, Yuri B et al. (2012). "The pulvinar regulates information transmission between cortical areas based on attention demands". In: *science* 337.6095, pp. 753–756.

Sullivan, Gail M and Richard Feinn (2012). "Using effect size—or why the P value is not enough". In: *Journal of graduate medical education* 4.3, pp. 279–282.

Xing, Dajun et al. (2012). "Laminar analysis of visually evoked activity in the primary visual cortex". In: *Proceedings of the National Academy of Sciences* 109.34, pp. 13871–13876.

Zhang, Lu et al. (2012). "Hippocampal theta-driving cells revealed by Granger causality". In: *Hippocampus* 22.8, pp. 1781–1793.

Brown, Harriet R and Karl J Friston (2013). "The functional anatomy of attention: a DCM study". In: *Frontiers in human neuroscience* 7, p. 784.

Markov, Nikola T and Henry Kennedy (2013). "The importance of being hierarchical". In: *Current opinion in neurobiology* 23.2, pp. 187–194.

Wang, Zheng et al. (2013). "The relationship of anatomical and functional connectivity to resting-state connectivity in primate somatosensory cortex". In: *Neuron* 78.6, pp. 1116–1126.

Giraldo, Luis Gonzalo Sanchez, Murali Rao, and Jose C Principe (2014). "Measures of entropy from data using infinitely divisible kernels". In: *IEEE Transactions on Information Theory* 61.1, pp. 535–548.

Markov, Nikola T, Julien Vezoli, et al. (2014). "Anatomy of hierarchy: feedforward and feedback pathways in macaque visual cortex". In: *Journal of Comparative Neurology* 522.1, pp. 225–259.

Bastos, Andre Moraes et al. (2015). "Visual areas exert feedforward and feedback influences through distinct frequency channels". In: *Neuron* 85.2, pp. 390–401.

Ray, Supratim (2015). "Challenges in the quantification and interpretation of spike-LFP relationships". In: *Current opinion in neurobiology* 31, pp. 111–118.

Herreras, Oscar (2016). "Local field potentials: myths and misunderstandings". In: *Frontiers in neural circuits* 10, p. 101.

Lundqvist, Mikael, Jonas Rose, et al. (2016). "Gamma and beta bursts underlie working memory". In: *Neuron* 90.1, pp. 152–164.

Pelt, Stan van et al. (2016). "Beta-and gamma-band activity reflect predictive coding in the processing of causal events". In: *Social cognitive and affective neuroscience* 11.6, pp. 973–980.

Kang, Daesung et al. (2017). "Reciprocal interactions between medial septum and hippocampus in theta generation: Granger causality decomposition of mixed spike-field recordings". In: *Frontiers in neuroanatomy* 11, p. 120.

Paneri, Sofia and Georgia G Gregoriou (2017). "Top-down control of visual attention by the prefrontal cortex. Functional specialization and long-range interactions". In: *Frontiers in neuroscience* 11, p. 545.

Bastos, André M, Roman Loonis, et al. (2018). "Laminar recordings in frontal cortex suggest distinct layers for maintenance and control of working memory". In: *Proceedings of the National Academy of Sciences* 115.5, pp. 1117–1122.

Choi, Hannah, Anitha Pasupathy, and Eric Shea-Brown (2018). "Predictive coding in area V4: dynamic shape discrimination under partial occlusion". In: *Neural computation* 30.5, pp. 1209–1257.

Hsieh, Han-Lin et al. (2018). "Multiscale modeling and decoding algorithms for spike-field activity". In: *Journal of neural engineering* 16.1, p. 016018.

Miller, Earl K, Mikael Lundqvist, and André M Bastos (2018). "Working Memory 2.0". In: *Neuron* 100.2, pp. 463–475.

Popov, Tzvetan, Ole Jensen, and Jan-Mathijs Schoffelen (2018). "Dorsal and ventral cortices are coupled by cross-frequency interactions during working memory". In: *NeuroImage* 178, pp. 277–286.

Richter, Craig G, Richard Coppola, and Steven L Bressler (2018). "Top-down beta oscillatory signaling conveys behavioral context in early visual cortex". In: *Scientific reports* 8.1, pp. 1–12.

Silverman, Bernard W (2018). *Density estimation for statistics and data analysis*. Routledge.

Akella, Shailaja and Jose C Principe (2019). "Correntropy based robust decomposition of neuromodulations". In: *2019 41st Annual International Conference of the IEEE Engineering in Medicine and Biology Society (EMBC)*. IEEE, pp. 5790–5793.

Gong, Xiajing, Wu Li, and Hualou Liang (2019). "Spike-field Granger causality for hybrid neural data analysis". In: *Journal of neurophysiology* 122.2, pp. 809–822.

Harris, Julie A et al. (2019). "Hierarchical organization of cortical and thalamic connectivity". In: *Nature* 575.7781, pp. 195–202.

Bastos, André M, Mikael Lundqvist, et al. (2020). "Layer and rhythm specificity for predictive routing". In: *Proceedings of the National Academy of Sciences* 117.49, pp. 31459–31469.

Lundqvist, Mikael, André M Bastos, and Earl K Miller (2020). "Preservation and changes in oscillatory dynamics across the cortical hierarchy". In: *Journal of cognitive neuroscience* 32.10, pp. 2024–2035.

Akella, Shailaja, Ali Mohebi, Jose C Principe, et al. (2021). "Marked point process representation of oscillatory dynamics underlying working memory". In: *Journal of Neural Engineering* 18.2, p. 026016.

Akella, Shailaja, Ali Mohebi, Kierstin Riels, et al. (2021). "Local power estimation of neuromodulations using point process modeling". In: *2021 10th International IEEE/EMBS Conference on Neural Engineering (NER)*. IEEE, pp. 420–425.

Akella, Shailaja and Jose C Principe (2021). "Neuromodulatory Pattern Analysis for Local Field Potentials". PhD thesis. University of Florida.

Ferro, Demetrio et al. (2021). "Directed information exchange between cortical layers in macaque V1 and V4 and its modulation by selective attention". In: *Proceedings of the National Academy of Sciences* 118.12, e2022097118.

Siegle, Joshua H et al. (2021). "Survey of spiking in the mouse visual system reveals functional hierarchy". In: *Nature* 592.7852, pp. 86–92.

Vezoli, Julien et al. (2021). "Brain rhythms define distinct interaction networks with differential dependence on anatomy". In: *Neuron* 109.23, pp. 3862–3878.

Dimakopoulos, Vasileios et al. (2022). "Information flows from hippocampus to auditory cortex during replay of verbal working memory items". In: *Elife* 11, e78677.

Jia, Xiaoxuan et al. (2022). "Multi-regional module-based signal transmission in mouse visual cortex". In: *Neuron* 110.9, pp. 1585–1598.

Semedo, João D et al. (2022). "Feedforward and feedback interactions between visual cortical areas use different population activity patterns". In: *Nature communications* 13.1, pp. 1–14.

Wang, Chuanmeizhi, Bijan Pesaran, and Maryam M Shanechi (2022). "Modeling multiscale causal interactions between spiking and field potential signals during behavior". In: *Journal of neural engineering* 19.2, p. 026001.

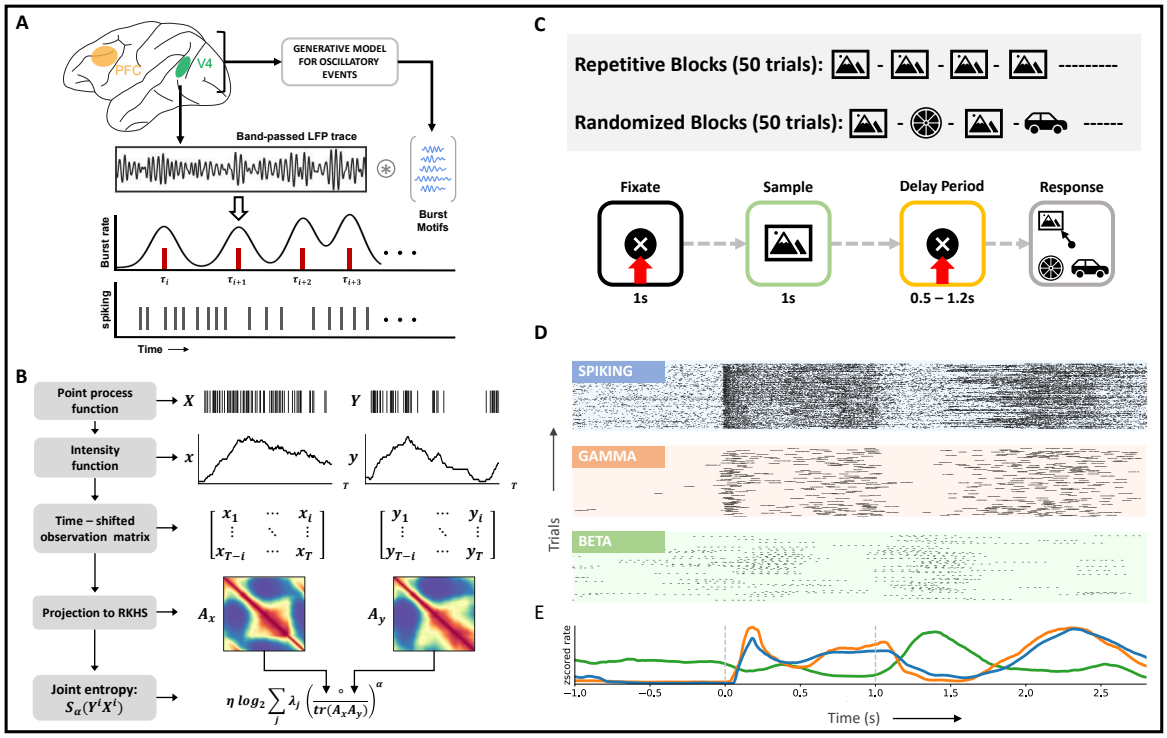

Figure 1: **Methods and behavioral task**. **A**, Mapping of local field potentials from continuous space to point process space. Using the generative model, a dictionary of typical oscillatory patterns is learnt from bandpassed LFP traces (training). Construction of the point process space for LFPs follows from a convolution between LFP traces and the learnt dictionary (testing).**B**, Example evaluation of joint entropy term in directed information (equation 16) using matrix formulation of Renyi's entropy, α-entropies. At time i, each time-shifted spiking matrix is projected onto a high–dimensional RKHS defined by the kernel, κ. Eigen-spectrum of the Hadamard product between the normalized Gram matrices captures the joint entropy between the two time series. **C**, (Top) Experimental setup. Following a 1s-fixation period, the subject is shown a sample stimulus for 1s. At the end of a delay period (fixed/variable), the subject saccades to the sampled stimulus that reappears at one of four randomized locations along with distractor images. **D**, Exemplar spiking activity and LFPs from layer 2/3 of V4 visualized in the same space of point processes, subject 2. For visualization purposes, every peak of the detected oscillatory burst has been demarcated. **E**, Multi-scale average rate plots obtained via kernel smoothing methods, subject 2. All activity is aligned with the trial intervals in **C**.

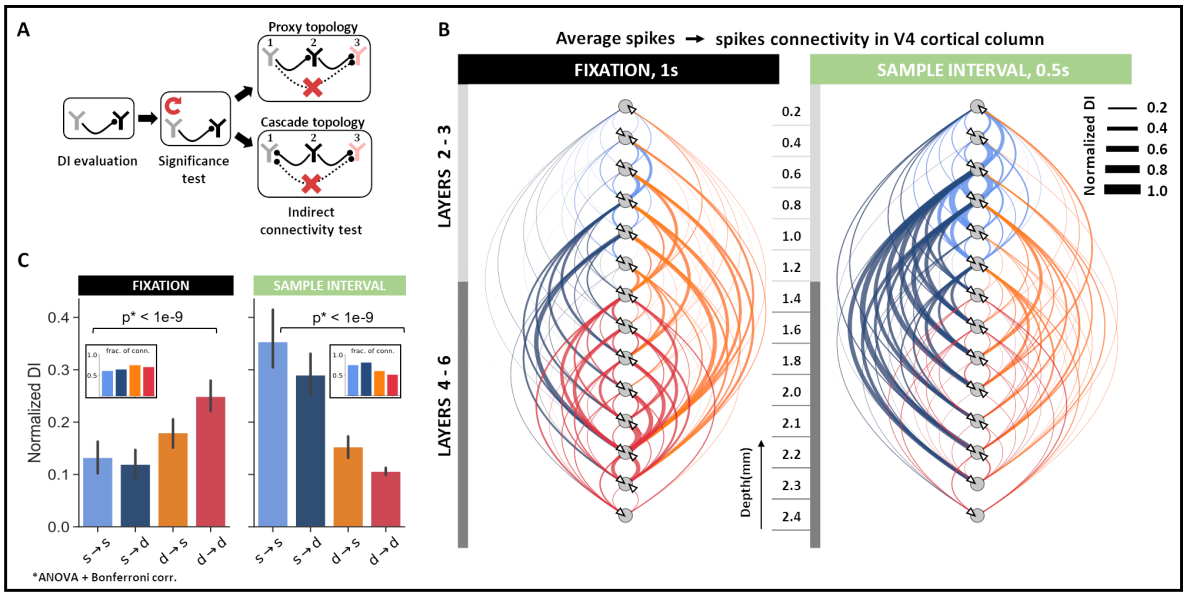

Figure 2: **Spike–spike interactions within cortical columns of V4**. **A**, Schematic to determine direct connectivity between neurons. Significant connectivities were identified against shuffled spiking in the causal neuron for $\alpha = 0.05$. Indirect connections were removed by systematically conditioning on neurons that formed cyclic connectivities. **B**, Direct causal influences between neurons in the V4 cortical column across all sessions (N = 123 units) during fixation (1s) and early sample (0.5s) intervals. Edges are weighted by the average DI between directly connected neurons at corresponding cortical depths. **C**, Connectivity trends between superficial (s, layers 2-3) and deep (d, layers 4-6) layer neurons in the fixation and early sample intervals. Mean ± SEM across all direct connectivity.

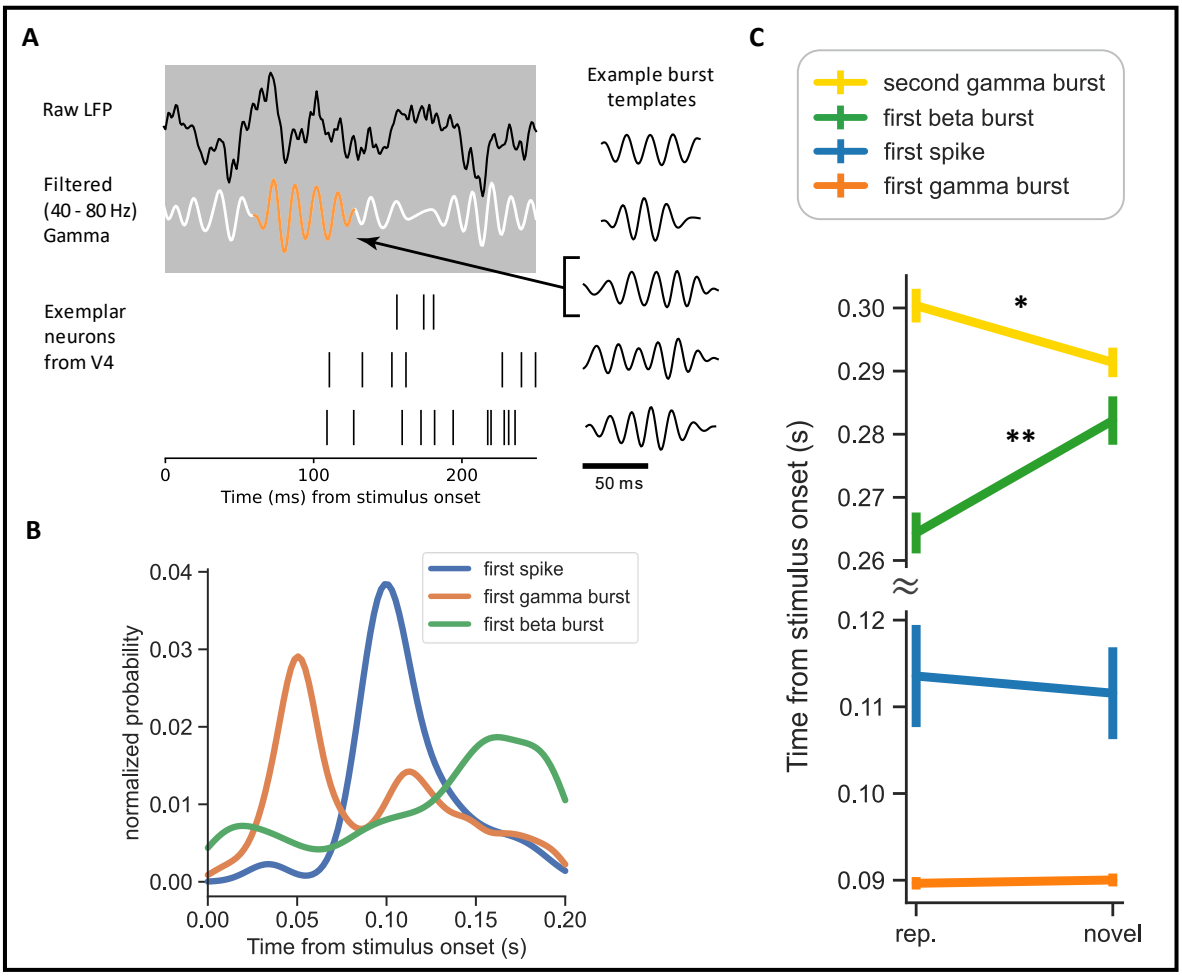

Figure 3: **Visually evoked onset response latencies in V4 spiking and LFP activity. A** Zoom-in on neural activity after stimulus onset indicating the dynamics of raw LFPs (black), gamma oscillations (white), gamma bursting (orange) and spiking activity. Right column highlights template that maximally match the gamma burst along with other example templates. **B**, Distribution of time to first spike/burst in response to sample stimulus across all units and layers in V4. **C**, Signal response latencies separated into trials of randomized and repetitive stimuli (*** $p < 0.001$). Error bars represent the 95% confidence interval.

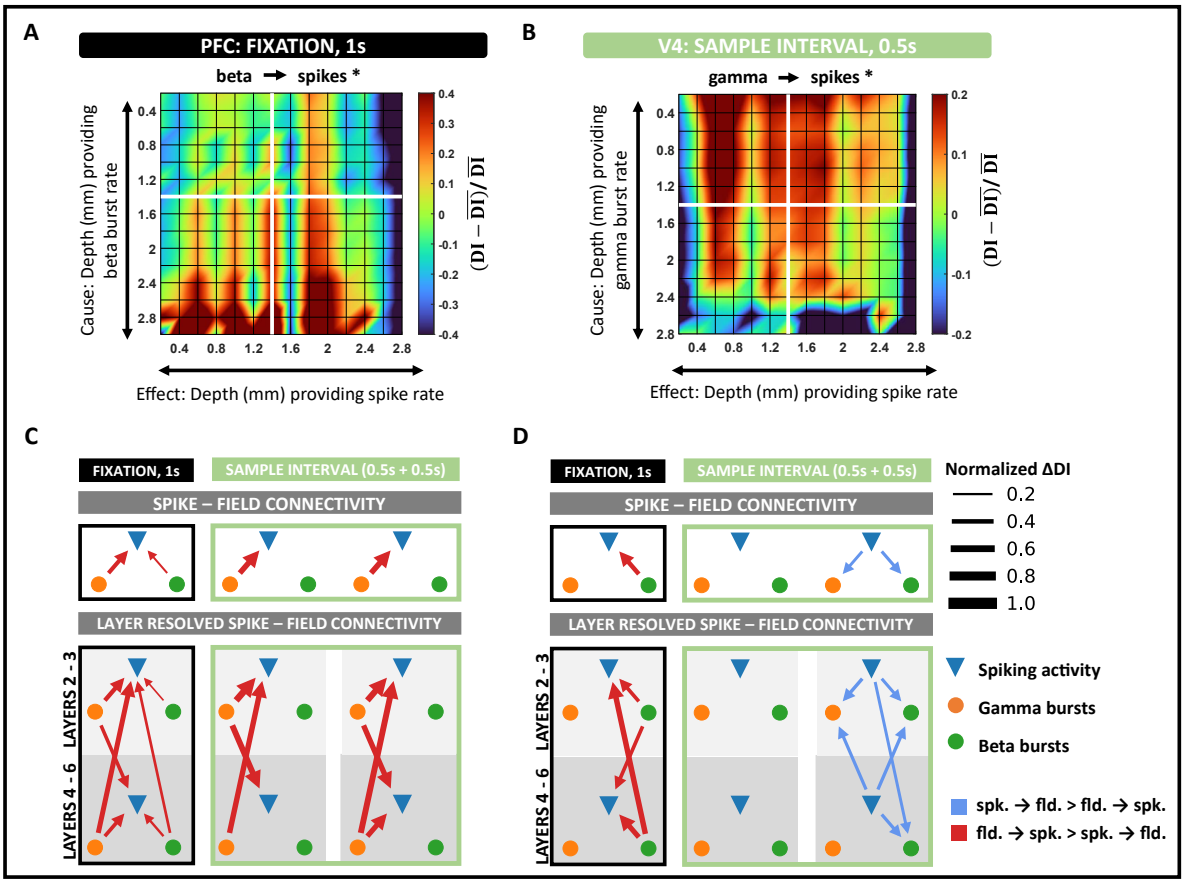

Figure 4: **Spike–field interactions within cortical columns of V4 and PFC. A**, Layer-specific connectivity plot in PFC from beta to spiking activity during the fixation interval (black asterisk denotes significant connection, $p < 0.001$ and Cohen d > 0.2). Color scale indicates the deviation of DI from the global mean DI across all layers. **B**, Layer-specific connectivity plot in V4 from gamma to spiking activity in the early sample interval (black asterisk denotes significant connection, $p < 0.001$ and Cohen d > 0.2). **C**, Intra – column spike – field connectivity in V4 during fixation and sample intervals. Significant connections identified as the dominant DI in opposite directions, spikes $\rightarrow$ fields and fields $\rightarrow$ spikes ($p < 0.001$ and Cohen d > 0.2). Edges are weighted by the absolute value of the difference in DI between opposite directions. **D**, Same as C, but in PFC.

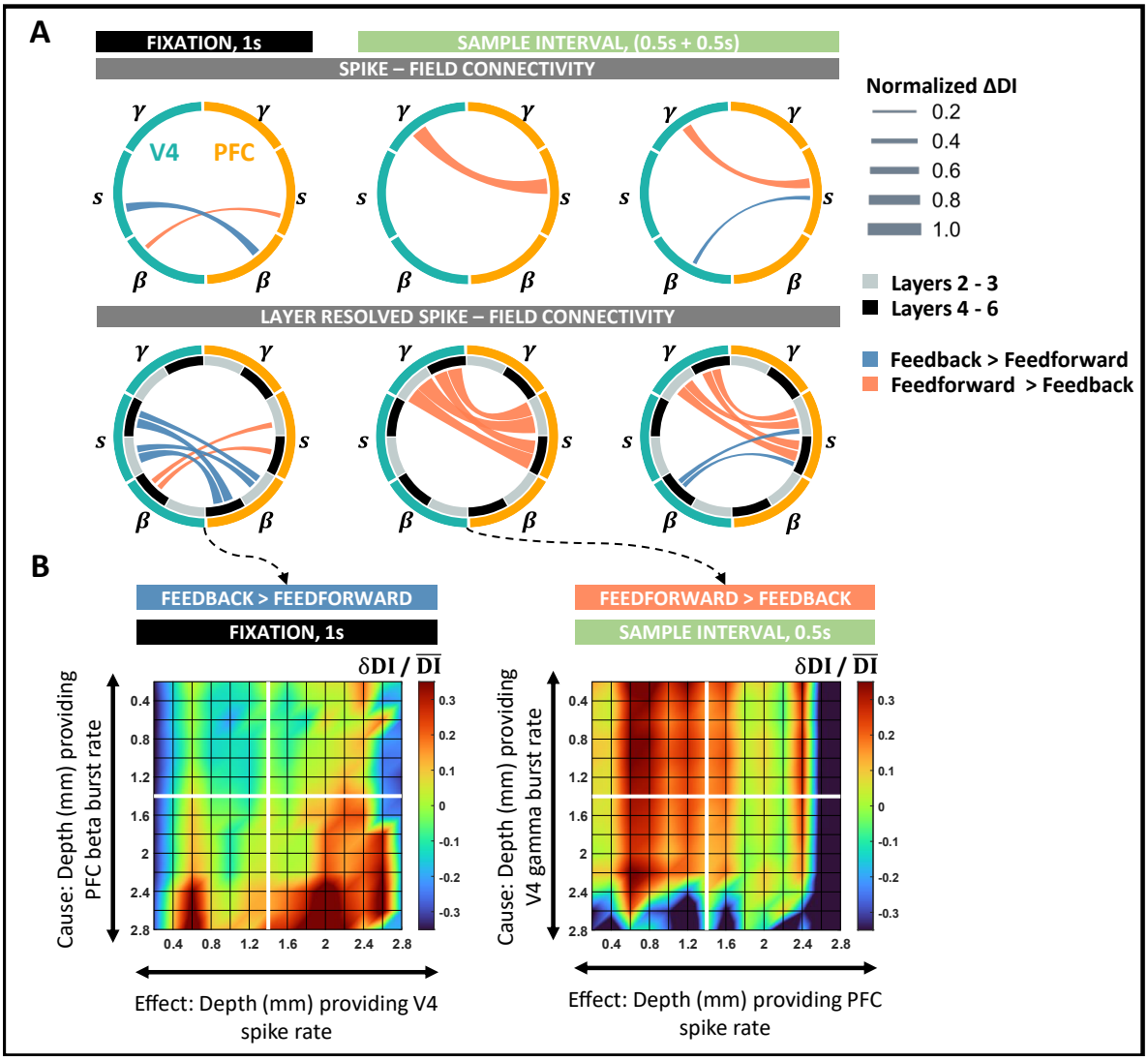

Figure 5: **Spike–field interactions between cortical columns of V4 and PFC. A**, (Top) Wheel plots summarizing significant feedforward and feedback spike – field connections between V4 and PFC during the fixation and sample intervals. Significant connections identified as the dominant DI in either direction of V4 → PFC and PFC → V4. (Bottom) Spike–field connectivity patterns between V4 and PFC layer resolved to deep (4-6) and superficial (2/3) interactions. **B**, Layer-specific connectivity plots between V4 and PFC for the most significant connections during fixation and sample intervals. (Left) Feedback connection from beta bursts in PFC to spiking activity in V4 during fixation. (Right) Feedforward connection from gamma bursts in V4 to spiking activity in PFC during the early sample interval. Color scale indicates the deviation of DI from the global mean DI across all layers. All significant connections were tested at $p < 0.001$ and Cohen d > 0.2. Edges are weighted by the absolute value of the difference in DI between opposite directions.

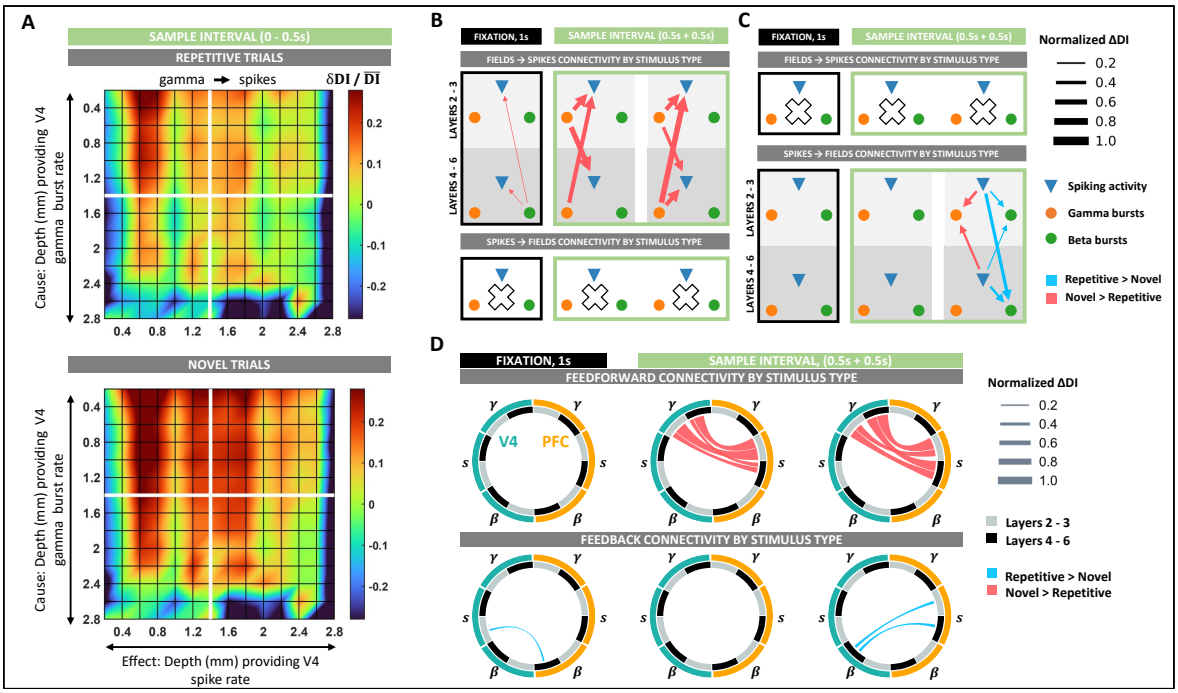

Figure 6: **Spike–field interaction patterns modulations by stimulus type.** **A**, Intra-column spike–field connectivity as modulated by stimulus predictability (randomized vs. repetitive) during fixation and sample intervals in V4 (top) and PFC (bottom). **B**, Spike–field connectivity between columns of V4 as modulated by stimulus predictability during fixation and sample intervals. All significant changes in DI between the trial groups of randomized and repetitive stimuli were tested at $p < 0.01$. Large white crosses denote an absence of significant modulations. Edges are weighted by the absolute value of the difference in DI between the two trial groups. **C**, Same as B, but in PFC. **D**, (Top) Wheel plots summarizing feedforward spike – field connections between V4 and PFC significantly modulated by sample predictability during the fixation and sample intervals. (Bottom) Same as top panel, but summarizing feedback connectivity significantly modulated by sample predictability.

5 Figures

6 Supporting Information

6.1 Figures

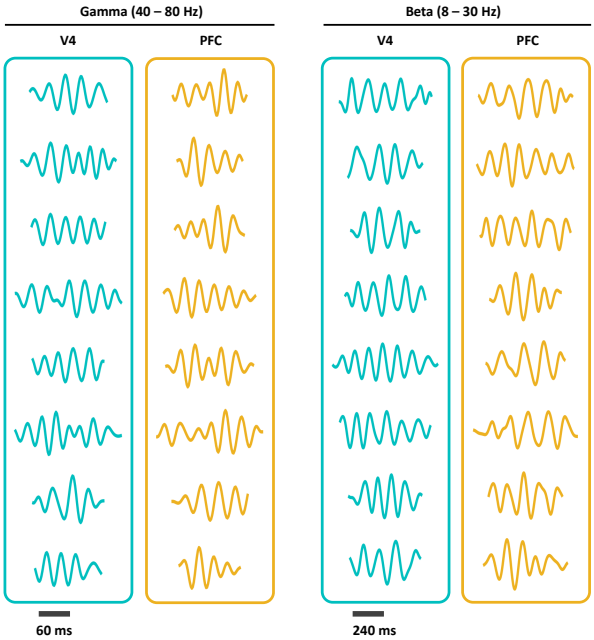

Figure S1: Example waveforms from the dictionary constructed using the generative model in the gamma and beta frequency ranges in the areas, V4 and PFC.

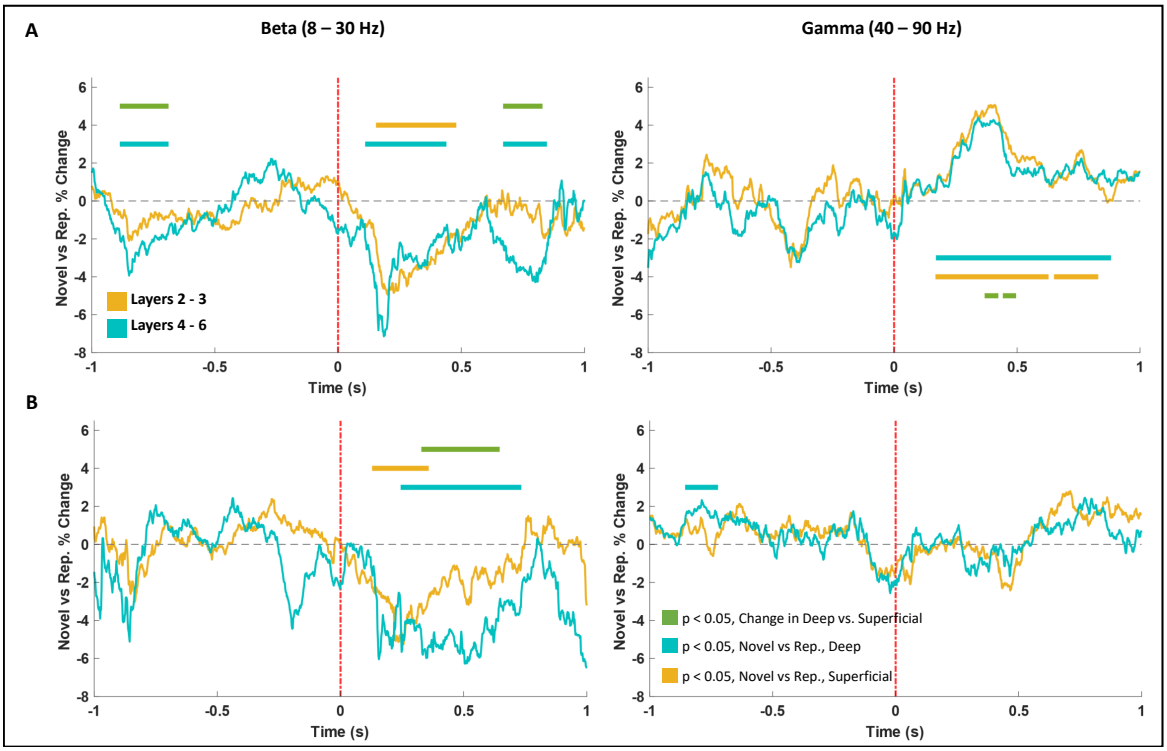

Figure S2: Change in instantaneous beta (column 1) and gamma (column 2) bursting power between randomized and repetitive trial blocks in **A** V4 and **B** PFC. Signals were analyzed during fixation, [-1, 0]s and stimulus processing [0, 1]s.

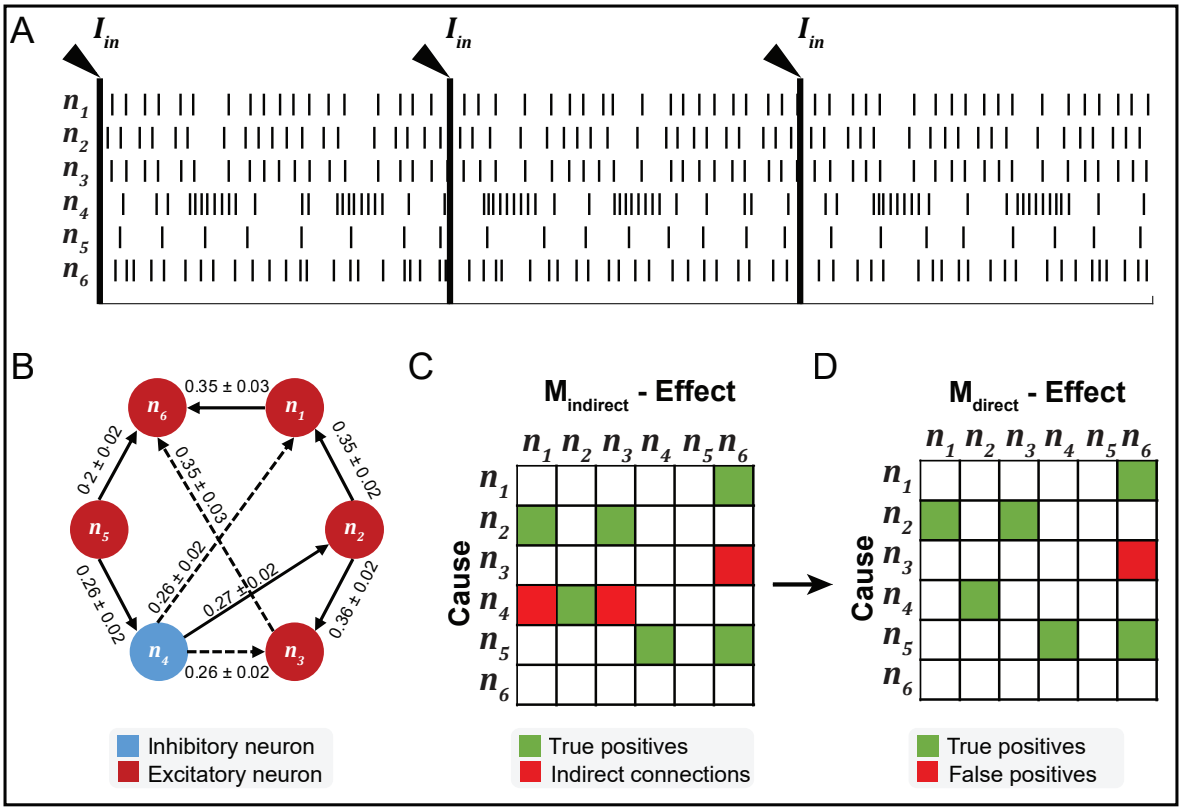

Figure S3: Identification of direct causal networks in a multi-neuron system. **A**. A1. Example data presenting 3 trials in each neuron. **B**. Network connectivity pattern and DI estimates for all directions identified by the model. Solid lines correspond to true direct causal directions, while dashed lines are indirect causal influences. **C** Estimated adjacency matrix including all causal influences, **D** Estimated adjacency matrix including only direct causal influences.

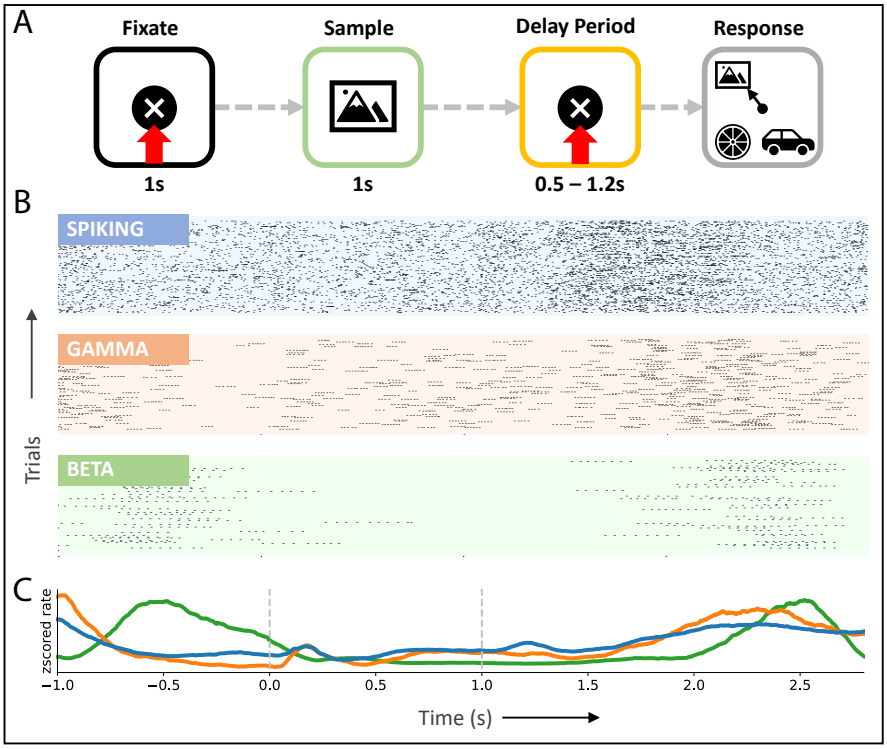

Figure S4: **A** Experimental setup. Following a 1s-fixation period, the subject is shown a sample stimulus for 1s. At the end of a delay period (fixed or variable), the subject saccades to the sampled stimulus that reappears at one of four randomized locations along with distractor images. **B**, Exemplar spiking activity and LFPs from layer 2/3 of PFC visualized in the same space of point processes, subject 2. **E**, Multi-scale average rate plots obtained via kernel smoothing methods, subject 2. All activity is aligned with the trial intervals in **C**.

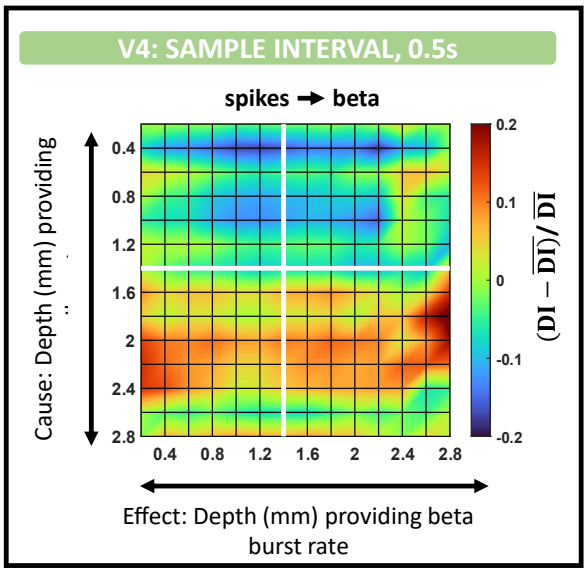

Figure S5: Spike → beta layer-wise connectivity plot in V4 during early sample interval.

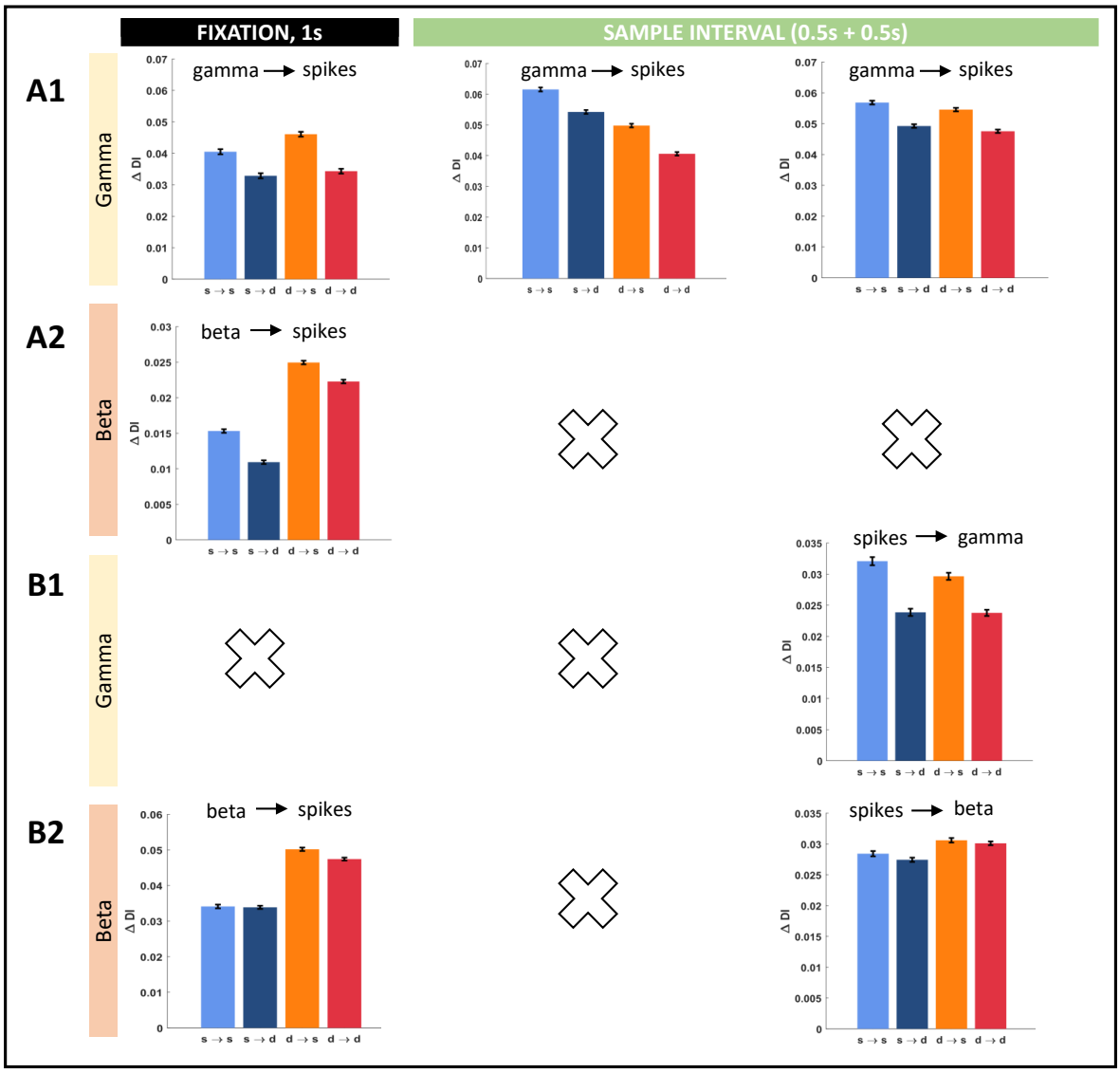

Figure S6: Summary of intralaminar spike-field connectivity patterns in **A** V4 and **B** PFC over fixation and stimulus presentation.

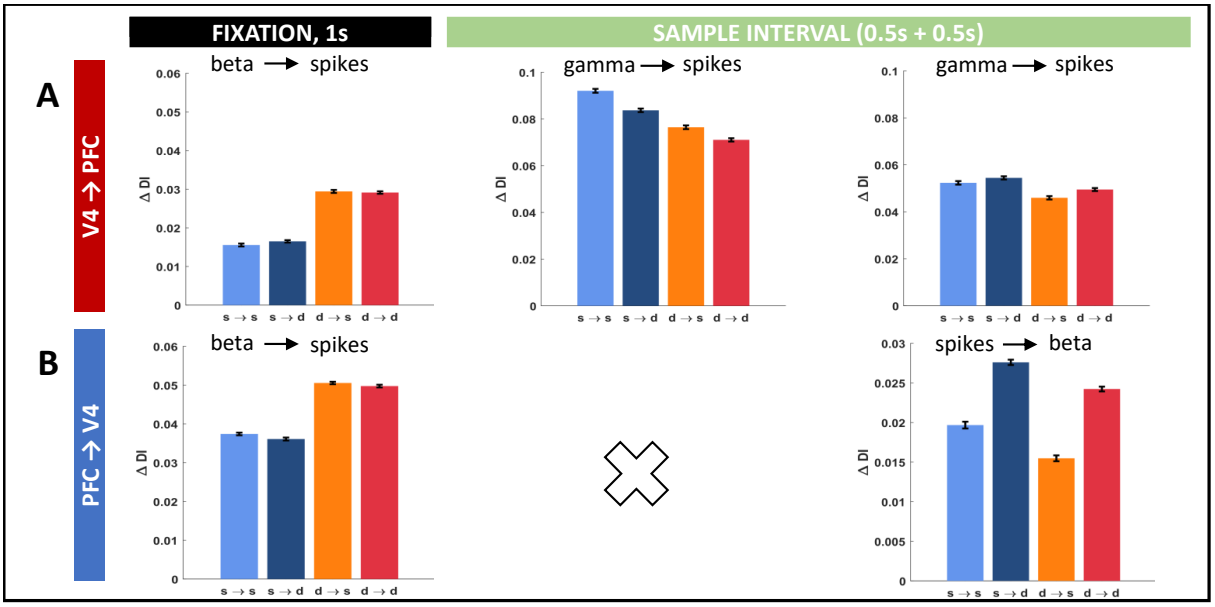

Figure S7: Summary of interlaminar spike-field connectivity patterns in the **A** feedforward (V4 → PFC) and **B** feedback (PFC → V4) directions during fixation and stimulus interval.

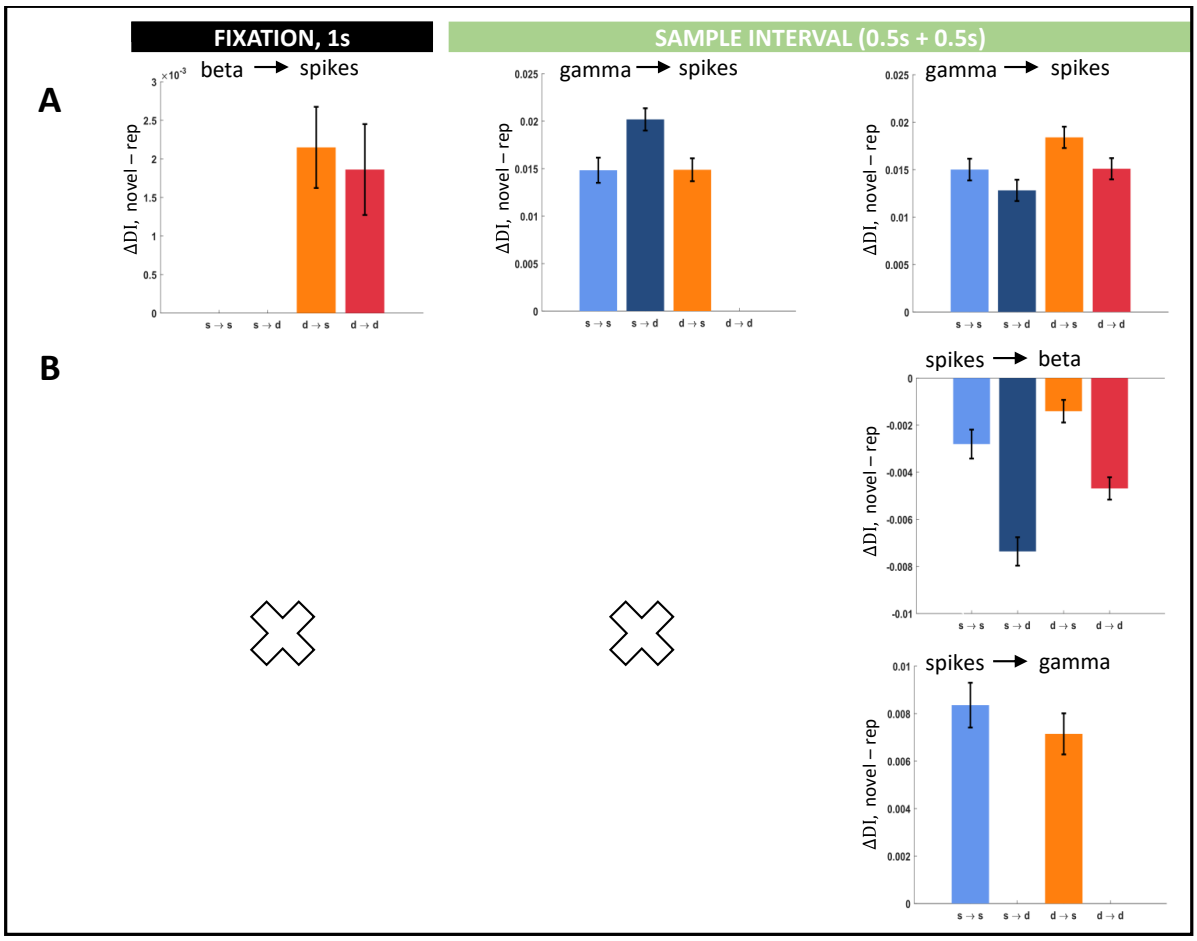

Figure S8: Effect of stimulus predictability on intralaminar spike-field connectivity patterns in the **A** V4 and **B** PFC during fixation and stimulus presentation.

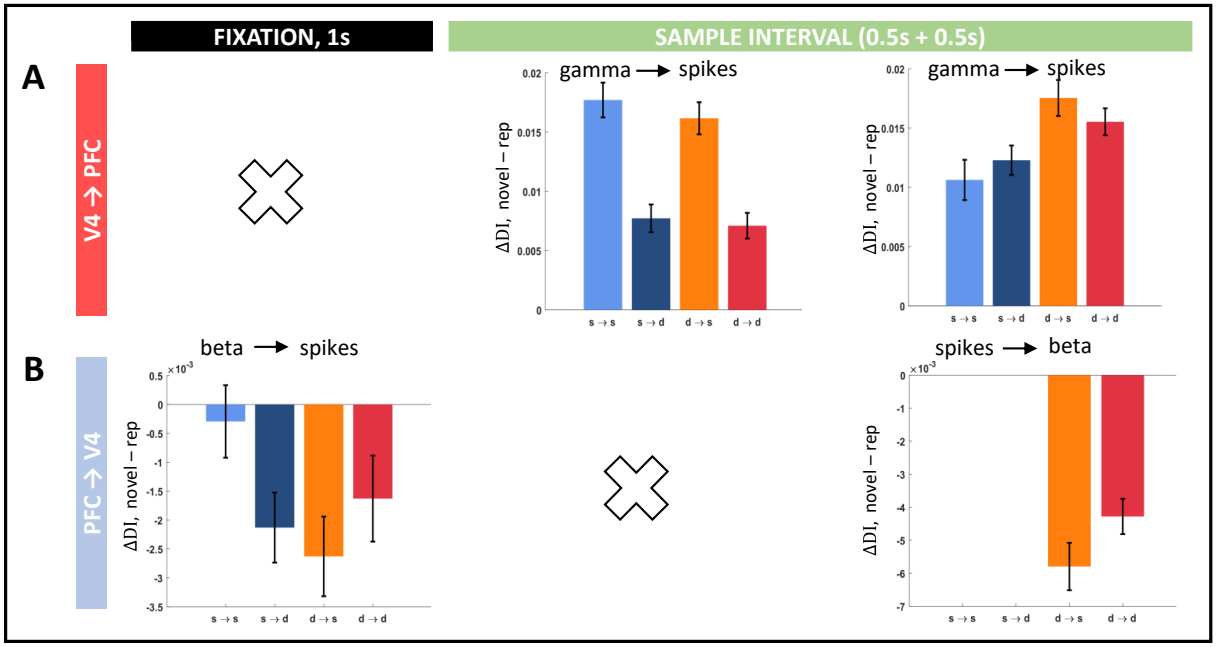

Figure S9: Effect of stimulus predictability on interlaminar spike-field connectivity patterns in the **A** V4 and **B** PFC during fixation and stimulus presentation.

6.2 Tables

Table S1: Izhikevich neuron model parameters for a regular spiking neuron

Model Parameter	**Variable**	**Value**
		voltages-mV, current-pA
Membrane Capacitance	C	100
Resting Membrane Potential	v_r	-60
Instantaneous Threshold Potential	v_t	-40
Peak Voltage	v_{peak}	35
Recovery Time Constant	a	0.03
Related to neuron's rheobase and input resistance	b, k	-2, 0.7
Voltage Reset Potential	c	-50
Net current flow during an action potential	d	100